On The Influence of Computed Tomography's Slice Thickness on Computer Tomography Based Finite Element Analyses Results

Leetal Eliyahu[1], Zohar Yosibash[1], Irit Avivi[2,3], Yael C. Cohen[2,3], Gal Ariel[2,4], Ofer Sadovnic[2,5] and Amir Sternheim[2,4]

[1] Computational Mechanics and Experimental Biomechanics Lab, School of Mechanical Engineering Tel-Aviv University, Israel.

[2]Sackler Faculty of Medicine, Tel Aviv University, Tel Aviv, Israel.

[3] Hematology Division, Tel Aviv Sourasky Medical Center, Tel Aviv, Israel.

[4] National Unit of Orthopaedic Oncology, Tel Aviv Sourasky Medical Center, Tel Aviv, Israel.

[5] Radiology Division, Tel Aviv Sourasky Medical Center, Tel Aviv, Israel.

Abstract

Background: Patient-specific autonomous finite element analyses of femurs, based on clinical computed tomography scans may be used to monitor the progression of bone-related diseases. Some CT scan protocols provide lower resolution (slice thickness of 3 mm) that affects the accuracy. To investigate the impact of low-resolution scans on the CT-based finite element analyses results, identical CT raw data were reconstructed twice to generate a 1mm ("gold standard") and a 3mm slice thickness scans.

Methods: CT-based finite element analyses of twenty-four femurs (twelve patients) under stance and sideways fall loads were performed based on 1 and 3mm slice thickness scans. Bone volume, load direction, and strains were extracted at different locations along the femurs and differences were evaluated.

Findings: Average differences in bone volume were 1.0±1.5%. The largest average difference in strains in stance position was in the neck region (11.0±13.4%), whereas in other regions these were much smaller. For sidewise fall loading, the average differences were at most 9.2±16.0%.

Interpretation: Whole-body low dose CT scans (3mm-slice thickness) are suboptimal for monitoring strain changes in patient's femurs but may allow longitudinal studies if larger than 5% in all areas and larger than 12% in the upper neck. CT-based finite element analyses with slice thickness of 3mm may be used in clinical practice for patients with smoldering myeloma to associate changes in strains with progression to active myeloma if above ~10%.

Keywords: Autonomous Finite Element Analysis, CT-based Finite Element Analysis, Femur, Multiple Myeloma, Slice Thickness

Introduction

Smoldering multiple myeloma (SMM) is a precancerous condition diagnosed by blood tests without symptoms of disease. SMM, often preceding active multiple myeloma (AMM), is defined in the presence of 10-60% clonal bone marrow plasma cells (BMPCs), but with no related organ damage (anemia, bone lytic lesions or renal failure). It accounts for 15% of newly diagnosed cases [19] and tends to progress over the years into AMM (the approximate time to progression being 10% per year throughout the first 5 years) [23]. The standard of care for SMM has been observation; nonetheless, randomized studies [25, 26] confirm the advantage of early intervention in reducing the risk of progression to AMM. Various methodologies have been proposed to identify SMM patients who are prone to develop AMM; however, current predictors[1] appear to be insufficiently sensitive (≤75%) [27] and none evaluate bone damage that might precede the detection of transformation to AMM. Research over the last decade noted the impact of bone's microenvironment in MM and its precursors, see [24]. It is conceivable that quantifying changes in bone stiffness over time for SMM patients may serve as a marker to identify patients who progress to AMM and potentially may benefit from an earlier treatment prior to the development of overt lytic bone lesions. Bone stiffness is quantified by performing finite element analyses based on CT scans [7,10], however the results depend on the resolution of the CT scans.

An autonomous CT-based finite element analysis (AFE) of the femurs, with no analyst intervention, named *Simfini*[2] was developed as a novel measure to accurately estimate bone strains (a quantified measure of bone stiffness and strength) [2]. *Simfini* removes analyst subjectivity, automatically segments the 3D model of the subject femurs and generates a patient-specific report on the femurs' strains for three different physiological loadings (stance position and two falling on the side). It is important to note that the segmentation in *Simfini* has been trained with CTs from different scanner and validated by experimental results using CT scans of lower abdomen including part of all femurs with a slice thickness/spacing of ≈1mm [7]. For example, a retrospective study using AFE on CT scans of patients with tumors demonstrated that 39% of patients may have had a more accurate diagnosis by considering

[1] Serum M-protein >2 g/dL (HR: 2.1), involved to uninvolved free light-chain ratio >20 (HR: 2.7), and marrow plasma cell infiltration >20% (HR: 2.4) [29]

[2] *Simfini* is a trademark of PerSimiO Ltd, Beer-Sheva, Israel.

AFE as a marker for a pathological fracture [13]. Such AFEs have also been used to assess the risk of osteoporotic fractures in type 2 diabetic patients, again based on opportunistic available CT scans [16].

As SMM patients routinely undergo a whole-body low-dose (WBLD) CT scan (slice thickness of 3mm) [28], one may assess bone stiffness changes via AFE and monitor MM evolution. A concept study explored the sensitivity and responsiveness of CT-based FEA in SMM patients to detect bone-disease progression, treatment response, and clinical correlates (a retrospective study of 16 MM patients that each had at least 2 consecutive CT scans of the spine and ~1/3 of the femur) [21]. The study showed promising trends with a monotonic increase in strain (denotes deterioration of bone strength) in AMM patients, a decrease in strain (implies bone strengthening) in patients who were responding well to treatment, and no changes in SMM patients that did not progress to AMM.

AFEs rely on a good resolution of the CT scan they are based on (usually having less than 1-2 mm slice thickness) which is usually not the slice thickness (ST) used in clinical practice for MM patients who undergo WBLD CT scans. This research thus concentrates on the influence of the axial resolution parameter, (ST) on the AFE results for both *Simfini-TUMOR* (AFE of the entire femur under stance loading conditions) and *Simfini-SENIOR* (AFE of the proximal femur under sidewise fall loading conditions). We focus on ST [6] and quantify differences in AFE results of femurs from CTs with two different STs (same raw data saved with variant ST and slice spacing - SS), specifically 3mm ST/1.5mm SS-which is often used in clinical practice compared to the 1mm ST/SS "gold standard". The goal, by using the same CT's raw data, is to keep all variables unchanged except one of interest, the ST, and quantify the percent difference between the AFE strains due to the change in ST. Only changes in strains above the determined differences, obtained by AFE of consecutive WBLD CT scans, may be considered significant to imply changes in the clinical situation for monitoring SMM patients.

Methods

CT-scans

WBLD CT scans of 20 patients were collected arbitrarily from the hospital's clinic registry at Sourasky MC for which the same raw data was available to generate CT scans with STs of 1, 2, and 3mm. Approval by the Sourasky MC institutional review board (0254-17-TLV) was granted. CT scans of 3mm ST are denoted "whole body low dose". All patients were scanned with a IQon - Spectral CT Phillips scanner, 120 kVP and kernel B reconstruction. All CT images reconstructed with a slice thickness of 1

mm were subsequently converted into 3mm thick slices to ensure that the CT raw data was identical for the various CT scans, i.e., each patient underwent a single CT scan that was post-processed to generate CT scans where the only varying factor is the ST/SS. The data of each patient and CT-scans are summarized in Table 1. Tumors were detected in the CT scans in some of these patients.

Table 1. Summary of extracted and eligible information for use in *Simfini*

Patient	*1*	*2*	*3*	*4*	*5*	*6*	*7*	*8*	*9*	*10*	*11*	*12*	*13*	*14*	*15*	*16*	*17*	*18*	*19*	*20*
Gender	M	F	M	F	F	M	M	M	F	F	F	M	M	F	F	F	F	M	M	M
Age	50	72	68	42	70	74	67	67	36	74	49	74	78	58	57	42	53	69	64	70
Weight (Kg)	75	**	87.5	59	67.5	69	66.5	79.5	47	63	74	80	100	72	71	89	70	**	80	82
Disease	**MM**	**MGUS**		**SMM**	**MM**		**SMM**	**MM**	**OS**	**MM**						**MM**	**MGUS**	**MM**		
1 mm	S	S	S L-Fs	S	S*	R-Fs L-I	S	S	S	S	S	NSS	NSS	NSS	NSS	S	S	S	S	Cf
SS	1	1	1	1	1	1	1	1	1	1	1	1	1	1	1	1	1	1	1	1
3mm	S	S	S L-Fs	S	S*	R-Fs L-I	S	S	S	S	S	NSS	NSS	NSS	NSS	S	S	S	Cf	Cf
SS	1.5	1.5	1.5	1.5	1.5	1.5	1.5	1.5	1.5	1.5	1.5	3	3	3	3	1.5	1.5	1.5	1.5	1.5

** Missing weight for patients 2 & 18, used the artificial weight of 60 kg to examine AFE differences. Diseases: MM-Multiple Myeloma, SMM-Smoldering MM, MGUS-Monoclonal Gammopathy, OS-Osteoarthritis.

R- Right femur, L- Left Femur, SS- Slice spacing: S-successful; I-Implant; Fs-Failed to segment; Cf-corrupt file, NSS-non-uniform slice spacing. *-alert of possible missing DICOM slice.

To represent "lower abdomen" typical CT scans (determining the risk of fracture in the elderly population), CT scans were also trimmed at 20 mm distal to the lesser trochanter, so the CT scan only represents the proximal femur as in [16]. These CT scans were used in *Simfini-SENIOR* to determine the *femoral bone strength with sidewise fall boundary conditions further described below*.

AFE Protocol

Simfini-TUMOR/SENIOR version V2.0.12 was used (see details in [2,5]). It allows an automatic mesh generation of tetrahedrals with curved boundaries with three optional mesh densities. These tetrahedral elements with curved surfaces are mapped to the standard element by blending functions so they accurately represent the bone surface. Over each element, the polynomial degree of the shape functions is increased from 1 to a maximum of 8 (the p-version of the finite element method), and numerical errors are evaluated (see [2] for further details). To assure minimal numerical errors, high mesh refinement was

used and the FE analyses were performed with a p-level of 8 providing an estimated relative error of less than 5%.

Segmentation

Simfini applies a machine learning algorithm to segment the femurs from a CT scan based on U-Net algorithm proved to be highly accurate in extracting the femur [22]. The U-Net also detects the slice that represents the end of the femur, as seen in Appendix D Figure D.1d for stance position, the slice that represents the end of the femoral head, Figure D.1c and thereafter the femurs are segmented, see Figure D.1b.

As most clinical CT scans do not use calibration phantoms, a phantom-less calibration was used to develop a linear relationship between Hounsfield units (HU) to longitudinal Young's modulus based on two values – the HU of air and the highest HU in patient's bone, assumed to correspond to the highest Young modulus of 20 GPa as described in [1]; any other HU represents a different longitudinal Young modulus by the relationships given in (1)-(4) together with Poisson's ratio ν = 0.3 [[1-2,9]. The value *a* in equation (1) is termed ``slope" and is determined from the HUmax allowing the use of relationships (1–4) to establish the longitudinal Young's modulus for all pixels [2].

(1) $\rho_{ash}\left[\frac{g}{cm^3}\right] = 0.877 \times 1.21 \times 10^{-3} \times a \times HU + 0.08$

(2) $E_{cort}\ [MPa] = 10200 \times {\rho_{ash}}^{2.01} \quad \rho_{ash} > 0.486\left[\frac{g}{cm^3}\right]$

(3) $E\ [MPa] = 2398 \quad 0.486\left[\frac{g}{cm^3}\right] \geq \rho_{ash} \geq 0.3\ \left[\frac{g}{cm^3}\right]$

(4) $E_{trab}\ [MPa] = 33900 \times {\rho_{ash}}^{2.2} \quad \rho_{ash} < 0.3\ \left[\frac{g}{cm^3}\right]$

Stance position FEA

A force of a magnitude equal to 2.5 body weights was applied to the femurs' head along a vector that connects the femur's head center and estimated intercondylar notch so to emulate a stance position [2]. These anatomical points were determined for each femur impacting the location at which force is applied on the head's surface. For each CT scan (1mm and 3mm) we monitored the volume of the femur, location of the anatomical points, as well as average principal strains at 6 different regions along the femur: the superior/inferior neck, trochanter, proximal shaft, middle shaft, and distal shaft shown in Figure 1. At

each region the maximum average tensile/compression principal strain over a 5 mm radius area around a local extremum was computed.

Figure 1. Regions of interest in CTFEA of the femur. Simfini-TUMOR produces a report with average max/min strains on the superior/inferior neck, trochanter, proximal shaft, middle shaft and distal shaft when a load is applied at the femoral head.

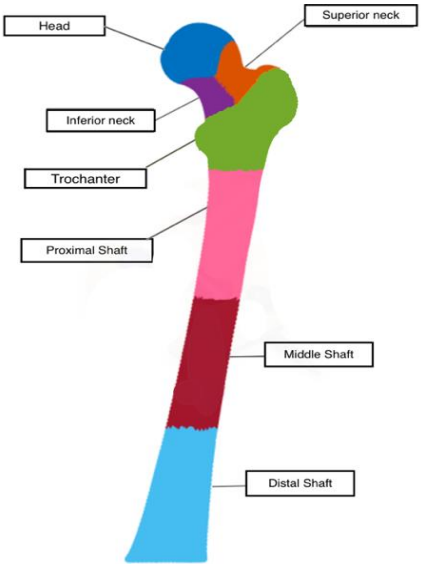

Fall on the side FEA

To represent a "lower abdomen" CT protocol the CT scan was trimmed at 20mm distally to the proximal trochanter. Such scans can be used to determine the risk of a hip fracture during sidewise falls in the elderly population [16]. *Simfini-SENIOR* applies three boundary conditions on the segmented femur, two loads which simulate sideways fall configurations applied at angles γ and δ, as well as stance position load as described above (here the intercondylar notch was estimated by a U-net algorithm), shown in Figure 2b. Neck fractures were associated with angles $\gamma_N = 10^\circ$ and $\delta_N = 15^\circ$ denoted as loading A or Fall A, while pertrochanteric fractures were associated with angles $\gamma_P = 30^\circ$ and $\delta_P = 45^\circ$ denoted as loading E or Fall E [18]. The regions in which strains were reported by the CTFEA are shown in Figure 2c.

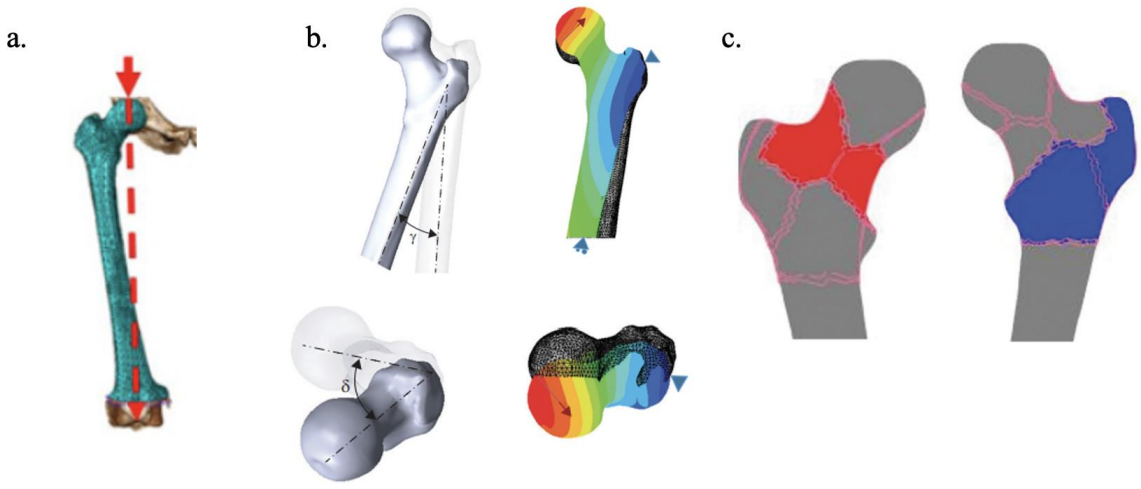

Figure 2. Representation of the force applied on the femur. a) Load applied at the femoral head during stance position at an angle dictated by the vector connecting the center of the femoral head and

intercondylar notch (determined by CNN when only a short bone is provided). b) Representation of angle γ (the angle between the femoral shaft and the ground during impact) and δ (the angle that reflects the internal or external rotation of the femur relative to the ground) that define the boundary conditions for sideways fall and dictate the direction of applied load for Fall A and Fall E. c) The area of interest when applying sideways fall boundary conditions: the femoral neck (Fall A) and the anterior and posterior trochanter (Fall E). Images from [16].

Data Assessment

The results of all loading conditions were used to assess the femurs' mechanical response. Computational time for the two femurs of each patient was ~1.5 hours for stance position and 3-4 hours for fall on the side due to additional loading directions. The time variant was due to the three loading conditions for fall on the side compared with the singular stance loading force. *Simfini* is autonomous without analyst intervention. Figure 3 provides an example of a partial report generated by *Simfini* for patient 4. Comparisons were performed for 1 and 3mm ST to qualify differences in AFE results. The percent change, defined by equations (5-7), was used as a quantitative measure at each location.

$$(5)\ Diff_{vol}(\%) \triangleq \frac{Vol|_{3mm} - Vol|_{1mm}}{Vol|_{1mm}} \times 100 \qquad vol = VV, MV$$

$$(6)\ Diff_{i}(\%) \triangleq \frac{E1|_{3mm} - E1|_{1mm}}{E1|_{1mm}} \times 100 \qquad i = SN, T, PS, MS, DS$$

$$(7)\ Diff_{i}(\%) \triangleq \frac{E3|_{3mm} - E3|_{1mm}}{E3|_{1mm}} \times 100 \qquad i = \frac{IN}{S}, T, PS, MS, DS$$

We denote the superior neck (SN), Inferior neck/ Subcapital $\left(\frac{IN}{S}\right)$ trochanter (T), proximal shaft (PS), middle shaft (MS), distal shaft (DS), voxel volume (VV), and mesh volume (MV).

Bland-Altman plots, defined and plotted by equations (19 & 20) in Appendix E, were used to display misbehavior of data: either bias, a trend, or inconsistent variability.

a.

b.

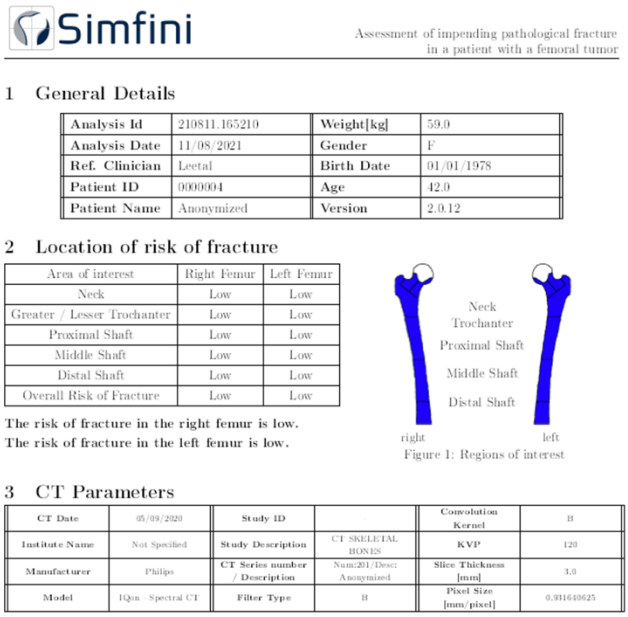

Simfini

Assessment of impending pathological fracture in a patient with a femoral tumor

1 General Details

Analysis Id	210811.165210	Weight[kg]	59.0
Analysis Date	11/08/2021	Gender	F
Ref. Clinician	Leetal	Birth Date	01/01/1978
Patient ID	0000004	Age	42.0
Patient Name	Anonymized	Version	2.0.12

2 Location of risk of fracture

Area of interest	Right Femur	Left Femur
Neck	Low	Low
Greater / Lesser Trochanter	Low	Low
Proximal Shaft	Low	Low
Middle Shaft	Low	Low
Distal Shaft	Low	Low
Overall Risk of Fracture	Low	Low

The risk of fracture in the right femur is low.
The risk of fracture in the left femur is low.

Figure 1: Regions of interest

3 CT Parameters

CT Date	05/09/2020	Study ID		Convolution Kernel	B
Institute Name	Not Specified	Study Description	CT SKELETAL BONES	KVP	120
Manufacturer	Philips	CT Series number / Description	Num:201/Desc: Anonymized	Slice Thickness [mm]	3.0
Model	IQon - Spectral CT	Filter Type	B	Pixel Size [mm/pixel]	0.931640625

4.2 Results table- Stance configuration

Description	Typical Value	Value		High Vs. Low	Strain fold Ratio		Body Weight to Fracture		Risk of Fracture	
		Right	Left		Right	Left	Right	Left	Right	Left
Max. tension strain (E1) @Superior neck [μS]	2850	2603	2305	0.13	0.91	0.81	7.01	7.92	Low	Low
Max. tension strain (E1) @Trochanter [μS]	1375	1155	1072	0.08	0.84	0.78	15.80	17.02	Low	Low
Max. tension strain (E1) @Proximal shaft [μS]	1375	1167	1044	0.12	0.85	0.76	15.64	17.48	Low	Low
Max. tension strain (E1) @Middle shaft [μS]	1325	794	785	0.01	0.60	0.59	22.98	23.26	Low	Low
Max. tension strain (E1) @Distal Shaft [μS]	625	424	375	0.13	0.68	0.60	43.07	48.70	Low	Low
Max. compression strain (E3) @Inferior neck/ Sub capital [μS]	-2750	-2370	-2303	0.03	0.86	0.84	9.07	9.33	Low	Low
Max. compression strain (E3) @Trochanter [μS]	-2100	-1864	-1755	0.06	0.89	0.84	11.54	12.25	Low	Low
Max. compression strain (E3) @Proximal shaft [μS]	-2100	-1679	-1718	0.02	0.80	0.82	12.81	12.52	Low	Low
Max. compression strain (E3) @Middle shaft [μS]	-1850	-1181	-1085	0.09	0.64	0.59	18.20	19.82	Low	Low
Max. compression strain (E3) @Distal Shaft [μS]	-1100	-843	-764	0.10	0.77	0.69	25.52	28.16	Low	Low
Total displacement (Utot) @Head center [mm]	-	3.21	2.82	1.14	-	-	-	-		
Bone Stiffness- Stability [N/mm]	-	460	523	1.14	-	-	-	-		

Simfini

Assessment of impending pathological fracture in a patient with a femoral tumor

Figure 3. An example of parts of *Simfini*'s report for the 1mm CT scan for patient 4. In (a) the general details of the patient are provided, a summary of the location of the risk of fracture is noted with an image generated to the right (blue depicts healthy regions while red denotes regions of risk), and the parameters of the CT scan are listed, (b) Displays a table where the rows show each region with strain values, the column shows what value is being calculated. The typical strains are the same for all reports and are the values of patients with healthy bones. The values in the second column were used as the strain values for each patient in equations (5-7) & (10-11).

Results

The results were based on scans for 13 patients, 1- 5, 7- 11, 16-18, who had consistent ST and SS within their CT scans (with 1 and 1.5 SS respectively) and underwent successful segmentation. Patient 6 had an implant in the left femur and was excluded. Patients 19 and 20 had corrupted files for either 1 or 3mm scans where the slice interval was irregular (missing a 2D slice in the femoral region) and thus could not be segmented properly, so were excluded. Patients 12- 15 did not have proper SS or ST for CT scans (were not in line with previous patients i.e., 3mm ST had SS of 3mm rather than 1.5mm), and thus were excluded. In addition, patient 3's left patella was not detected properly during segmentation in *Simfini-TUMOR* and the results for the right femur were incomplete and so patient 3 was extracted from the stance position data. Patient 16 did not segment properly in *Simfini-SENIOR* due to a dividing voxels error which has already been addressed in a more recent version of *Simfini*.

Table 1 shows the summary of information that was extracted and eligible for use based on the subset provided; patients marked in grey were used in this report for both loading conditions. Patients marked in blue were only used for stance loading, whereas patients marked in green were only used in fall on the side loading conditions. I.e., the information was based on 24 femurs (12 right femurs and 12 left femurs).

Simfini-TUMOR (Stance Position Loading)

The segmented volume (i.e., voxel volume) and the mesh volume (composed of tetrahedral elements) had a < 2% increase in the stance position, Figure 4. Here the left femur of patient 10 shows >11% change, this is due to improper detection of the final slice of the distal shaft in 3mm ST CT (further explained below and shown in Figure D.2). The 3mm ST scans result in most cases a larger volume compared to 1mm ST scans.

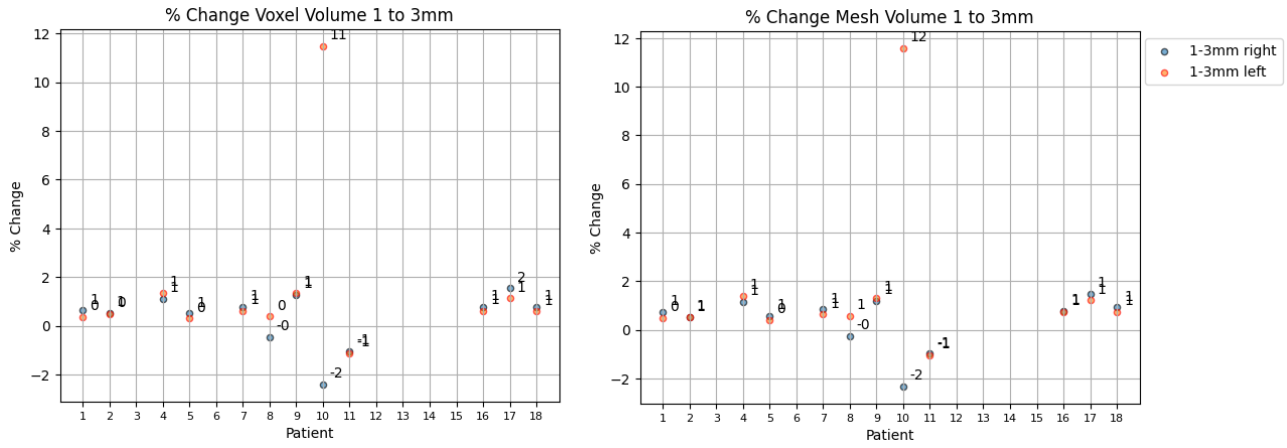

Figure 4. Percent change of voxel and mesh volume between 1 and 3mm scan for each segmented femur.

Graphs in Figure 5 show the percent change of strains from 3 to 1mm (for patients 1, 2, 4, 5, 7-11, 16-18) based on the 6 regions shown in Figure 1. The differences were calculated according to (6-7), where E1 denotes the average maximum principal strain (tension) and E3 denotes the minimum principal strain (compression) at every given region *i*. A large variation was noticed in the superior neck with ~30% change from 1mm to 3mm. For the trochanter a difference of 15% or less is noticed overall in stance position. In the proximal shaft and middle shaft, we see ≤16% and ≤9% difference respectively. In the distal shaft we noticed a ~20% difference. An outlier in all regions was noted for patient 8 presumably due to slope detection (addressed below and explained in Appendix B). The total displacement of the head center was ~5% with an outlier for patients 2 and 8 right and left femur respectively with >10% difference. Similar patterns were seen in bone stiffness where patients 2 and 8 are outliers (graphs can be

found in Figure A.1 in Appendix A). The compression principal strains, which follow similar patterns as the tension strains, are available in Appendix A in Figure A.3.

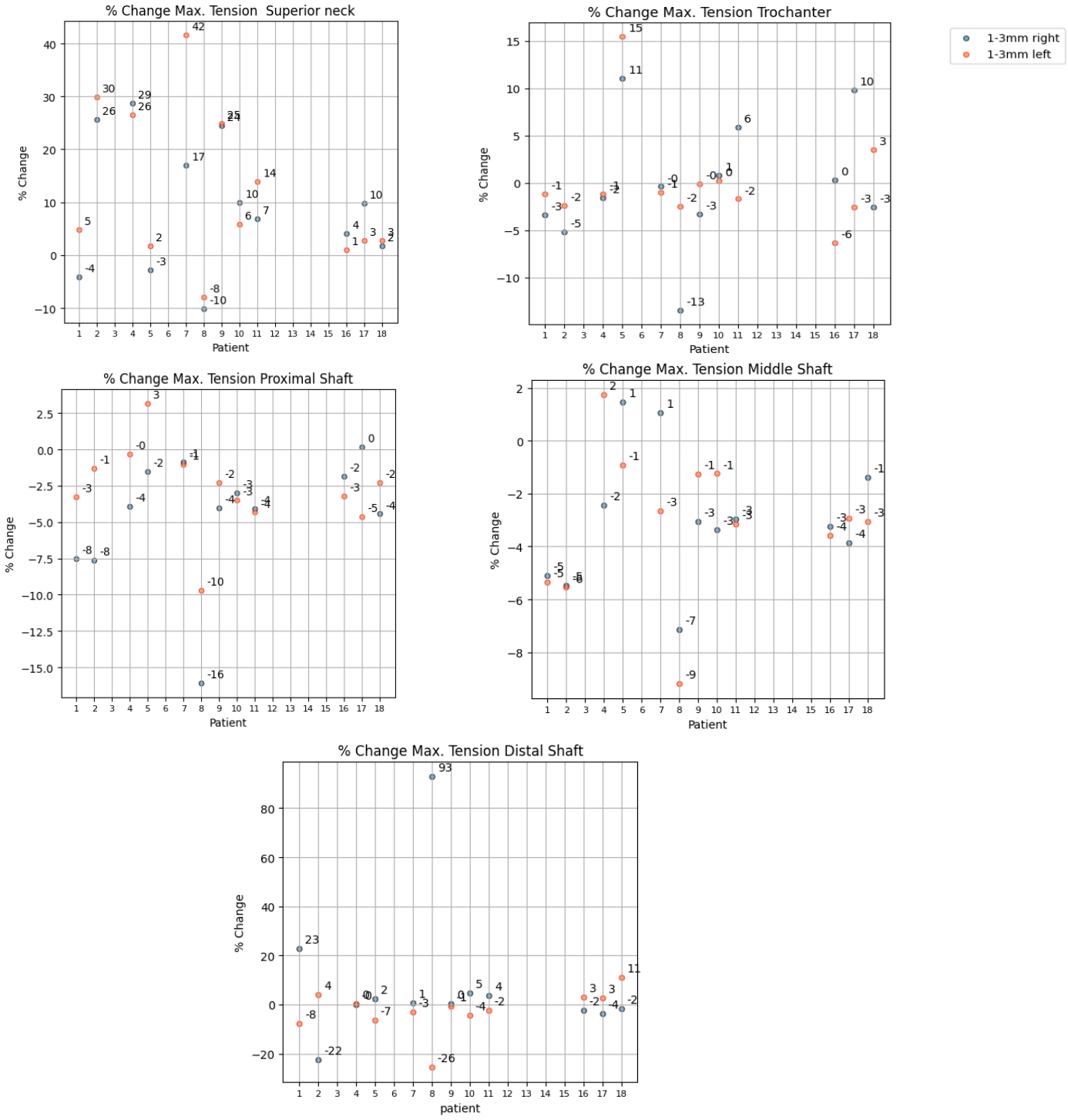

Figure 5. Percent change of the average principal strain at the superior neck, trochanter, proximal shaft, middle shaft, and distal shaft for each segmented femur.

Since loading direction (determined by the anatomical points) affects the strains, we investigated whether inaccuracies of anatomical points are evident. The difference in the coordinates of the head center and the intercondylar notch was computed by (8) and plotted in Figure 6. Overall, the difference in distance was ~4mm, except for patient 2's right femur as well at the detection of patient 10's anatomical points for the left femur in both the head center and intercondylar notch.

(8) $Diff.in\ Distance_{\ i} = \sqrt{(x_{3mm} - x_{1mm})^2 + (y_{3mm} - y_{1mm})^2 + (z_{3mm} - z_{1mm})^2} \quad i = HC_{x,y,z}; IC_{x,y,z}$

(9) $$Diff.in\ Distance_{\ HC-IC} = \left[\left(\sqrt{(x_{IC} - x_{HC})^2 + (y_{IC} - y_{HC})^2 + (z_{IC} - z_{HC})^2}\right)_{3mm} - \left(\sqrt{(x_{IC} - x_{HC})^2 + (y_{IC} - y_{HC})^2 + (z_{IC} - Z_{HC})^2}\right)_{1mm}\right]$$

We denote the coordinates of the Head Center (HC) and the coordinates of the intercondylar (IC).

a.

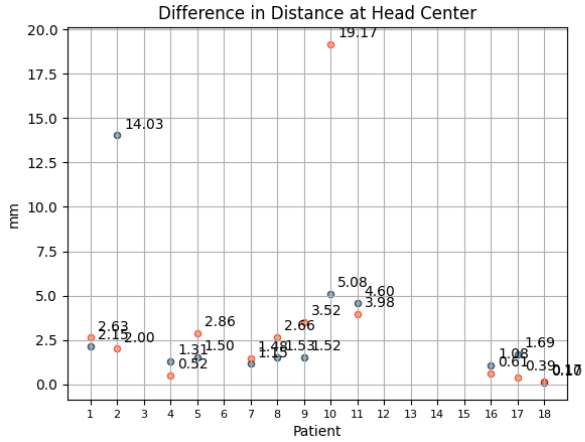

b.

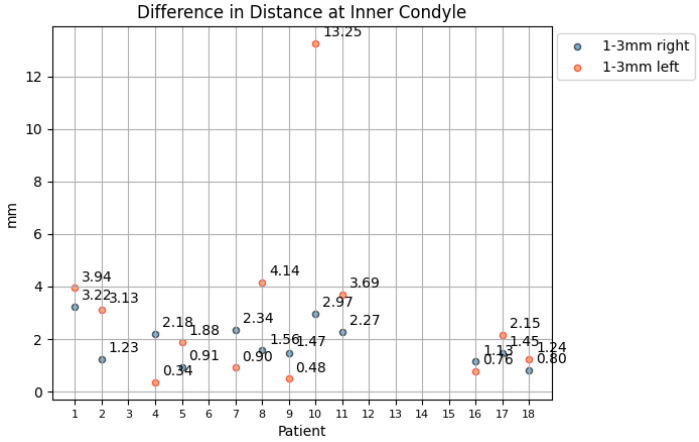

Figure 6. The graphs above show the difference in distance (in millimeters) of the a) head center in 1-3mm scans and b) the intercondylar region from 1-3mm.

The distance from head center to intercondylar notch was calculated by (9) and plotted in Appendix A Figure A.2. This distance affects the loading vector.

As the direction of applied load affects the strains, we investigate how the angle at which the load was applied changes and if the change in degrees affects the variations in strains. The angles were calculated

based on (10)-(14). The angle at which load was applied is marginally changed when comparing ST as shown in Figure 7.

(10) $Vector_i = (x_{IC} - x_{HC}, y_{IC} - y_{HC}, z_{IC} - z_{HC}\ )\ i = 1mm; 3mm$

(11) $Length_{Vector\ i} = \sqrt{(x_i)^2 + (y_i)^2 + (z_i)^2} \qquad i = 1mm; 3mm$

(12) $Dot\ product_{1mm \cdot 3mm} = Vector_{1mm} \cdot Vector_{3mm} = (x_i \times x_j) + (y_i \times y_j) + (z_i \times z_j)$
$i = Vector_{1mm};\ j = Vector_{3mm}$

(13) $Length_{1mm * 3mm} = Length_{Vector\ 1mm} \times Length_{Vector\ 3mm}$

(14) $Change\ in\ Angle = \left(\cos^{-1}\left(\frac{Dot\ product_{1mm \cdot 3mm}}{Length_{1mm * 3mm}}\right)\right) \times \frac{180}{\pi}$

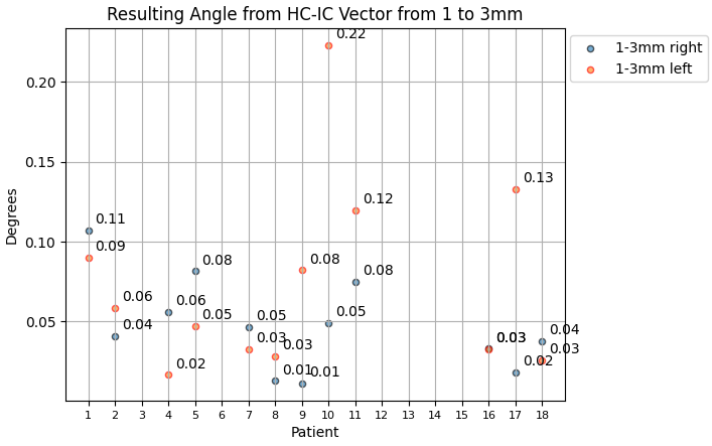

Figure 7. The change in degrees from 1mm vs. 3mm of the angle at which the loading vector was applied.

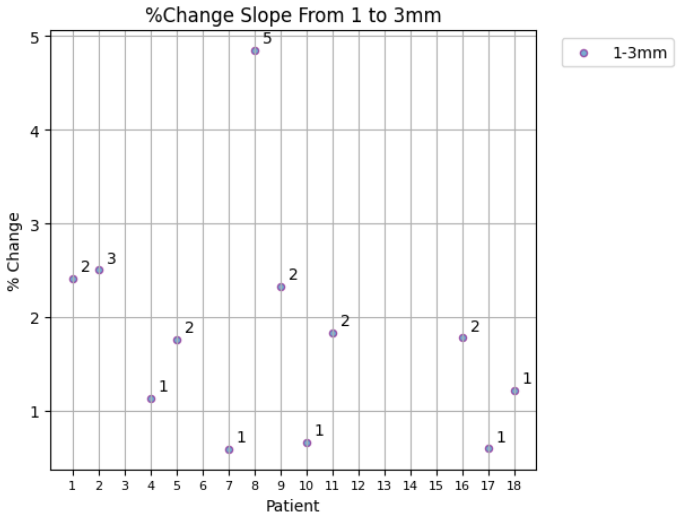

Figure 8. Change in slope *a* between 1mm & 3mm scans.

As the Young modulus is based on HU see equation (1), we investigated the slope *a* of each femur calculated during segmentation. Differences in said slope can account for variations seen in 1 to 3mm analysis (see Figure 8). A higher percentage change of slope from 1-3mm was noted for patient 8 which may explain the large difference in strains noticed for this patient. We address this specific patient in Appendix B.

To consider a global measure for whole patients**,** we computed the average percentage change and standard deviation among all patients and all femurs at the specific locations, see Table 2. This average was taken to understand the underlying trends in our data, whereas the standard deviation depicts the dispersion of measurements relative to the average. Here we see the largest average % change in the superior neck with ~11% and a standard deviation of ~±14%. For the trochanter, proximal shaft, and middle shaft the average % change was <-5% with a standard deviation of < ±7%.

$$(15)\ \text{Avg. Change}_i = \sum_{j=1}^{n} \frac{(Diff_i)_j}{n}$$

$$(16)\ \textit{Standard}\ \text{Deviation}_i = \sqrt{\frac{\sum_{j=1}^{n}\left((Diff_i)_j - \bar{x}\right)^2}{n-1}}$$

where i=location, $Diff_i$= % change of strain value from 1mm to 3mm of the patient (j) at each location (i), $\bar{x}$= the mean of $Diff_i$, and n= total number of femurs.

Table 2. The average difference and standard deviation at each location are 1mm to 3mm for *Simfini-TUMOR*. Calculations by (15) & (16).

	Average % Change ± Std		
	1 to 3mm		
	Slopes	1.8 ± 1.2	
	Femur	Right; n= 12	Left; n= 12
	Angle	0.0 ± 0.0	0.1 ± 0.1
Volume	Voxel	0.3 ± 1.1	1.5 ± 3.2
	Mesh	0.4 ± 1.1	1.5 ± 3.2
Distance	Head Center	3.0 ± 3.8	3.3 ± 5.2
	Inner Condyles	1.8 ± 0.8	3.0 ± 3.5
	Head Center to Inner Condyles	-1.4 ± 4.7	0.0 ± 4.2
Max. Tension Strain % Change (E1)	Superior Neck	9.3 ± 12.5	12.3 ± 14.9
	Trochanter	0.0 ± 5.4	-0.2 ± 6.7
	Proximal Shaft	-4.6 ± 4.3	-2.7 ± 3.0
	Middle Shaft	-3.0 ± 2.5	-3.1 ± 2.8
	Distal Shaft	2.4 ± 12.3	-2.4 ± 8.9
Max. compression strain % Change (E3)	Inferior Neck/ Subcapital	7.5 ± 8.4	3.3 ± 5.7
	Trochanter	-4.6 ± 5.6	-3.8 ± 6.9
	Proximal Shaft	-2.4 ± 4.8	-3.4 ± 4.6
	Middle Shaft	-3.1 ± 2.8	-3.3 ± 4.2
	Distal Shaft	-3.8 ± 3.4	-3.5 ± 6.1
Total displacement (Utot) @Head center [mm] % Change		-3.9 ± 4.2	-3.5 ± 4.0
Bone Stiffness-Stability % Change		4.2 ± 4.9	3.8 ± 4.5

Simfini-Senior Fall on The Side Loading

Simfini-SENIOR was distinguished as applying 3 various loads on the femoral bone providing three FEA results for 3 instances of applied loading directions. The differences were calculated according to (6-7), where Figures 9 and 10, representing Fall A and Fall E respectively, show a percentage change in compression strain (compression forces due to impact load are of interest here).

Figure C.2 in Appendix C shows a percentage change for tension and compression in stance position in the regions of the femoral neck and trochanter. Stance position data are of less interest here as we are specifically interested in sidewise fall.

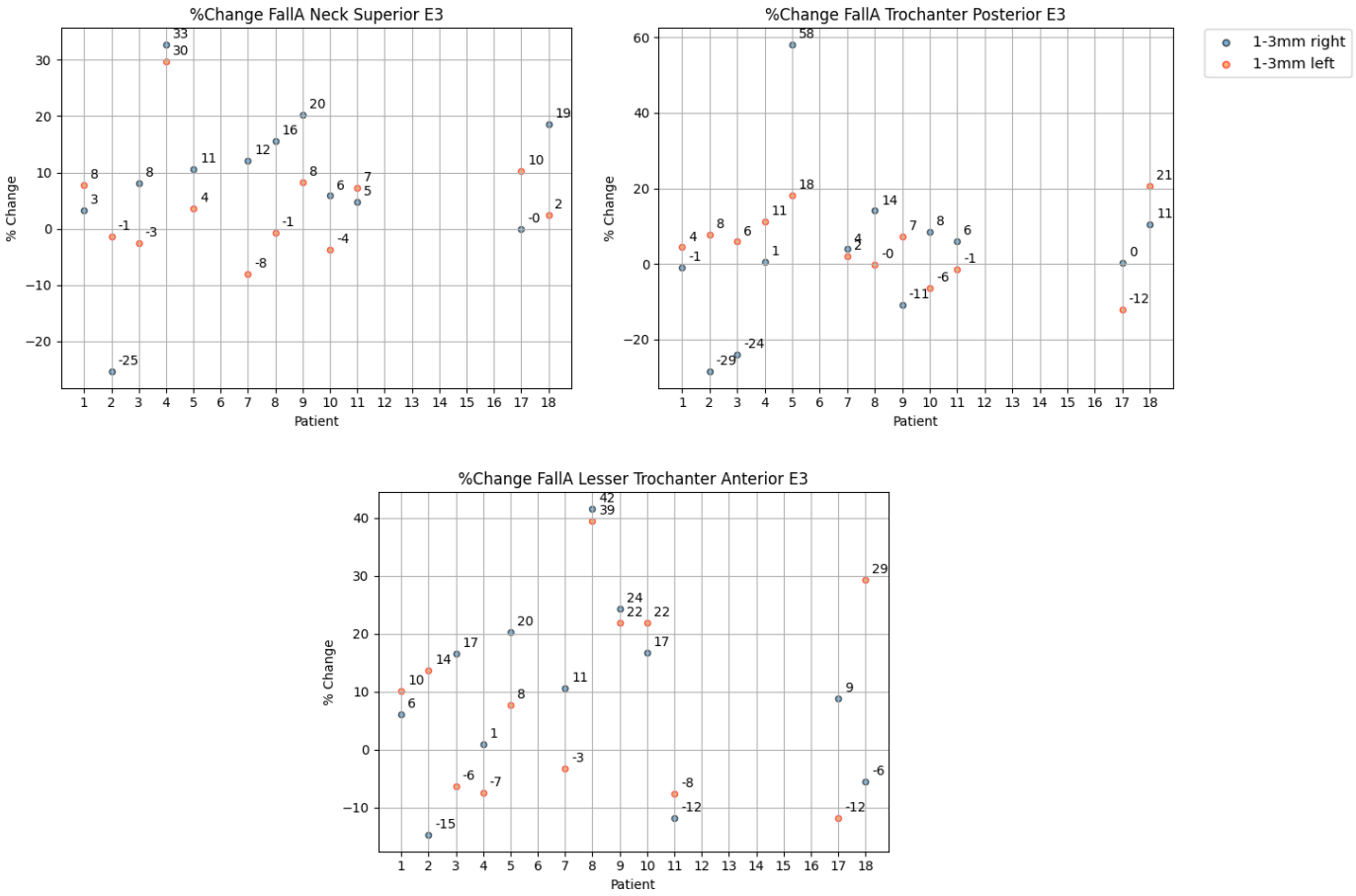

Figure 9. Percent change of the average compression strain at the superior neck, trochanter posterior, and trochanter anterior for each segmented femur with loading conditions applied at Fall A orientation.

Figure 9 represents Fall A loading representing impending neck fractures. Differences in the superior neck range ~-8-20% with a noted outlier for patient 2 of 33% & 30% for the right and left bone respectively. Large differences were seen in the trochanter posterior with >25% for patients 2 and 5 as well as in the trochanter anterior exceeding a 20% in this region.

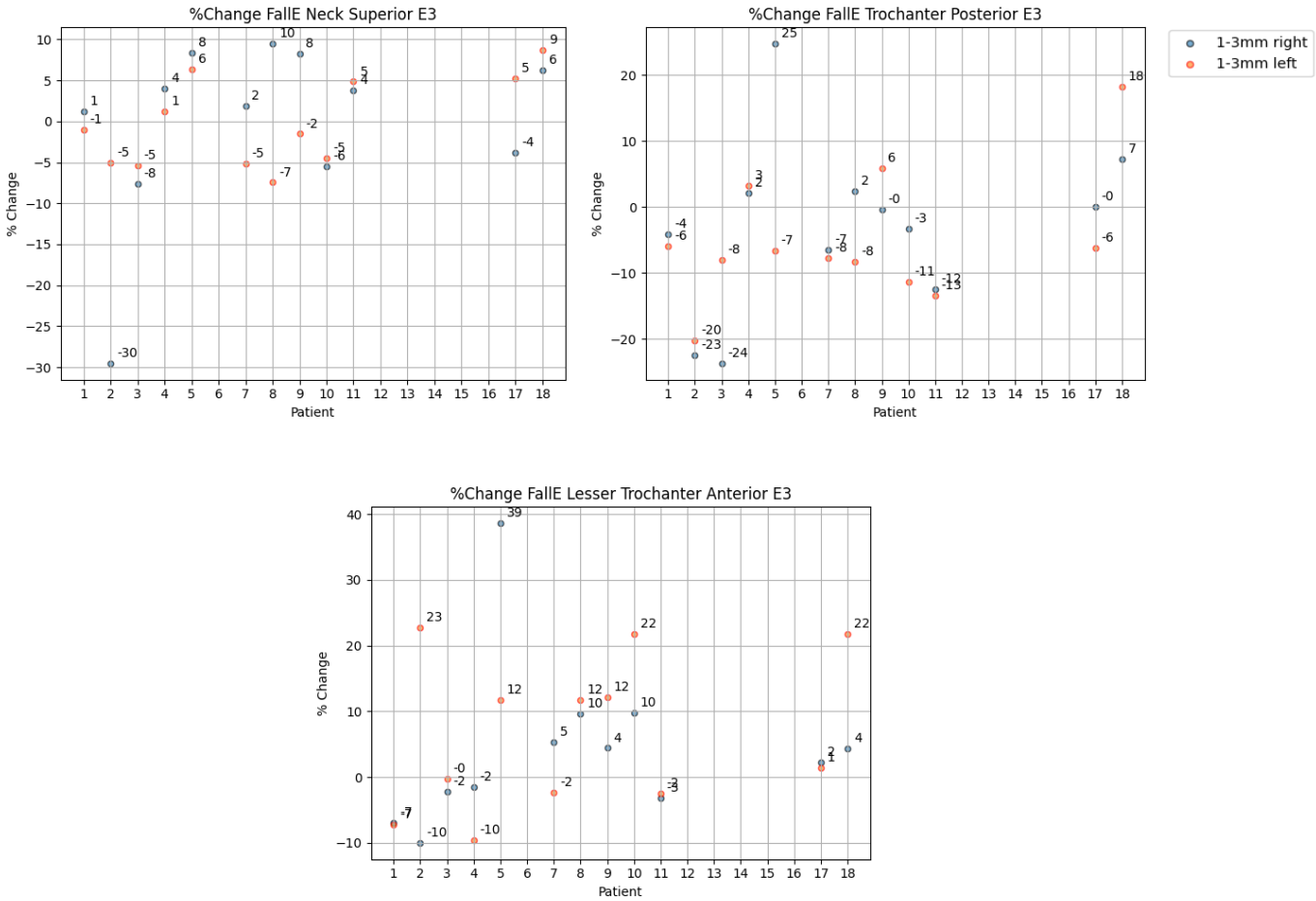

Figure 10. Percent change of the average compression strain at Fall E loading conditions at the superior neck, trochanter posterior, and trochanter anterior for each segmented femur.

Figure 10 shows Fall E loading conditions representing impending pertrochanteric fractures. Here the superior neck region shows a ≥10% change, noting a larger difference for the right femur of patient 2. Large differences were seen in the trochanter posterior with >25% for patients 2,5, and 17 as well as in the trochanter anterior exceeding 20% in this region.

When comparing the slope acquired to assess bone density, larger differences were noted, specifically for patients 2, 10, and 18 shown in Figure 11 below. These differences can greatly impact FEA outcome, as noted above for patient 8 in stance position loading and can explain the larger percent differences noted in fall on the side FEA analysis.

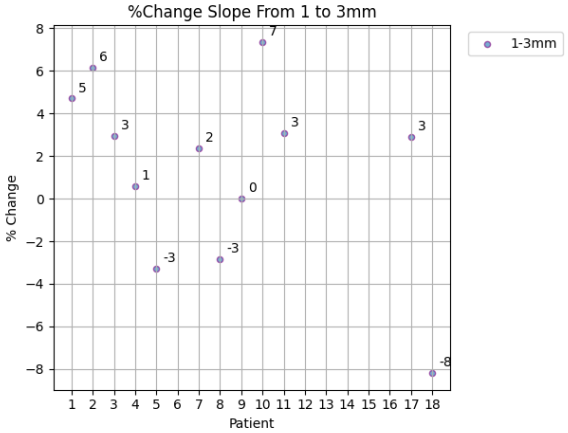

Figure 11. % Change in slope for 1mm & 3mm ST.

Table 3. Average difference and standard deviation at each location 1mm to 3mm for *Simfini-SENIOR*. Calculations by (15) & (16).

	Average % Change ± Std		
	1 to 3mm		
	Slopes	1.3 ± 4.4	
	Femur	Right; n= 12	Left; n= 12
Max. compression strain % Change (E3) Fall A	Neck Superior	8.9 ± 14.0	4.4 ± 9.7
	Trochanter Posterior	3.1 ± 21.7	4.7 ± 9.4
	Trochanter Anterior	9.5 ± 16.0	9.0 ± 16.7
Max. compression strain % Change (E3) Fall E	Neck Superior	-0.3 ± 10.8	-0.3 ± 5.5
	Trochanter Posterior	-3.1 ± 13.0	-5.1 ± 10.0
	Trochanter Anterior	4.2 ± 12.5	6.8 ± 11.7
Max. Tension Strain % Change (E1) Stance Position	Neck Superior	9.9 ± 11.4	12.4 ± 14.3
	Trochanter	1.6 ± 9.2	0.8 ± 8.0
Max. compression strain (E3) Stance Position	Inferior Neck/ Subcapital	6.4 ± 8.3	5.4 ± 6.8
	Trochanter	-4.6 ± 9.1	-2.2 ± 11.3
Total displacement (Utot) @Head center [mm] % Change		-1.7 ± 9.9	-0.7 ± 6.7
Bone Stiffness-Stability % Change		2.7 ± 11.5	1.1 ± 6.6

To consider a global measure along short bones**,** average % change and standard deviation among all patients were computed, see Table 3. The averages and standard deviation were computed according to

(15-16). Here we see an average of <10% difference for Fall A, with a large standard deviation ranging from 8-24%. For Fall E a lower average of <6% was seen with a STD of up to 15.5%.

Bland Altman plots in Appendix F, show a constant bias for all regions in both stance position and for fall on the side, without detection of a proportional error or inconsistent/erratic variability. The intervals of agreements were spread out, yet 95% of the data lay within ±1.96 SD of the mean difference. The bias, lower, and upper limits are displayed in Table F.1 as a precent deviation based on the difference of means. For stance position a constant bias of ≤ 6.6% is noted for the trochanter, proximal shaft, and middle shaft in tension and compression with large standard deviations, whereas the superior neck and distal shaft resulted in larger biases with a larger standard deviation. A constant bias of ≤10% for Fall on the Side was noted. The nature of the Bland-Altman plot resulted in difficulty to decern if, causing the large deviations detected along various regions, were consistent with one patient.

Discussion and Conclusions

Here AFE results for low-resolution WBLD CT scans (3mm ST), common for SMM patients, were compared with those obtained via standard-resolution CT scans (1mm ST). The percentage difference serves for quantifying the changes in longitudinal studies above which should be considered significant for SMM patients.

Studies on the impact of phantom vs phantomless calibration on FEA results [30] indicated that fracture risk prediction was very similar (within an 80% range) [30]. More recently, Ataei et al (2022) [31] evaluated the effects of altered CT scan protocol's on FEA failure load assessment by phantom and phantomless calibration. Five cadavers' femurs were scanned 8 times for varying protocols: phantoms or phantomless; tube current (mA), peak kilovoltage (kVp), slice thickness (ST), rotation time, field of view (FOV), reconstruction kernel, and reconstruction algorithm were investigated. Variations in ST of 1mm compared to 3mm ST are reported to have ~±10% variations in failure load. The study did not consider stiffness at various regions nor being the ST the only changed parameter (multiple scans of the same bone alter CT imaging results [29, 32]). Our study is the first, to our knowledge, to compare the influence of ST in clinical CT scans of 13 patients generated from same raw data on bone strains in different regions and phantomless calibration.

AFE produced segmented femurs where the differences in mesh volume followed the same patterns as voxel volume for all scans, concluding that the mesh represents the femurs' geometry well. The bone volume difference between 3 to 1mm ST was insignificant with an average difference after meshing of 0.4 ± 1.1% for the right femur and 1.5 ± 3.2% for the left. Accurate slice range detection of the femur did not have to be precise: for example, although a large percent change was noted for the left femur of patient 10 (~12% difference) the percentage change in stains did not appear to be greatly affected. This is because the anatomical points were adjusted with the volume. The reason for the segmentation discrepancy was a part of the knee, which was included in the 3mm ST scan, see Figure D.1. These changes in volume and adjustments of anatomical points at which loading was applied marginally affected the direction angle of load with an average 0.1% change in the angle direction. Thus, we found that ST had a minimal effect on segmentation and any changes due to segmentation seemed to be negligent in affecting stains.

In some rare instances (as in patient 2's right femur) due to the automatic segmentation the femur head may be geometrically distorted changing the dimensions of head and the associated anatomical points, impacting orientation of applied load. This caused the larger difference seen in bone stiffness, as shown in Figure A.1 (right). Both 1mm and 3mm ST segmented bones for patient 2 were equally distorted, the automatic segmentation could not detect the beginning of femoral head properly in both instances due to the many tumors in the femoral head.

The slope depends on the number of pixels with high HU values, so a lower resolution CT impacts the maximum HU value, so impacting the HU to ash density calibration. Thus, differences in the slope value (5% for example for patient 8 in stance position and 6.2% for patient 2 in sidewise fall) lead to notable changes in strains among various regions throughout the femur. Calibration appeared most significant in strain deviations. *It is important to improve the slope estimation to reduce the differences among different CT scans.* Investigation of other methods in patient specific calibration, such as that in [31], is warranted in future studies to assess variation in the methodology of phantomless calibration.

Interestingly, when the total displacement at the head center in stance position was assessed, see Appendix A Figure A.1, patients 2 and 8 stood out as problematic. Patient 2 is due to the distorted head and patient 8 is due to the slope. This was also the case for sidewise fall analyses, where all patients with a larger % change in slope experienced larger % change in total displacement at the head center, see Appendix C Figure C.1(left).

For the *Simfini-TUMOR* analyses (for which the entire femur is visible in the CT scan), the strains exhibited an overall difference of about 5% except at the neck where differences were about 12%. The standard deviation tended to be large, with femurs for which a 30% difference is noticed at the neck, as large as 10% difference was noticed at the trochanter and at the proximal and middle shaft a smaller difference of 5% were observed. The large differences in the femoral neck were due to the overlooked cortical shell in the superior neck, which is ~1mm thick (longitudinally), in CT scans with a ST of 3mm this cortical shell may have been partially or completely missed. Holzer et al. 2009 conducted a study demonstrating that in the femoral neck the cortical bone and its geometry are primarily responsible for the bone strength [12]. Thus, scans that "overlooked" the cortical bone may provide an inaccurate representation of the femur's bone strength this location. This is clearly seen in Figure 5 for the region of the superior neck where strains for 3mm ST scans were much higher than those in 1mm scans (represented by the positive % change) meaning that the system estimated a much weaker bone in this region. For the trochanter, proximal shaft, and middle shaft the average % change is <-5% with a standard deviation of <±7% in tension and compression denoted that on average at lower resolutions produced strains in tension and compression that tended to be lower, thus interpreting a higher bone strength. The positive % change in the superior neck compared to the overall negative % change noted in all other regions signified that in lower resolution the analysis detected a stronger bone apart of the super neck where, due to this missed cortical bone, bone strength is interpreted to be much weaker. Treece et al. 2012 presented a model-fitting algorithm that allows for the accurate estimation of cortical bone thickness by identifying sub millimeter cortical shell via a fixed cortex density having promising results for missed cortical shell correction [11]. Missed cortical shell detection is more pronounced in low-resolution CT scans making conclusive observations the superior neck non-optimal. To attempt at providing better biomechanical interpretation at the superior neck, Treece's methods will be implemented in *Simfini* and further assessed in the future.

The distal shaft is highly affected by the fixation or "clamping" of the femur that caused singular artifact stresses which are wrongly detected as a maximum stain. The large difference in this region was not of great concern as typically femoral bones do not fracture in this region, unless a large tumor exists which would be detected visually.

For the *Simfini-SENIOR* analyses (for which only the proximal femur is visible in the CT scan) smaller variations for the two loading conditions (Fall A and Fall E) were visible for the compressive strains. The overall percentage change is mostly below 10% difference. Larger variations were noted in the lesser trochanter anterior for both Fall A and Fall E, with overall better correlations between the two resolutions

seen for Fall E boundary conditions compared to Fall A. Possibly, as Fall A simulates impact at the femoral neck, the "overlooked" cortical shell (as mentioned above) may greatly impact interpreted bone stiffness yielding varying outcomes compared to Fall E which simulates impact at the trochanter posterior and anterior. Stance position loading results showed similar tends as seen in *Simfini*-TUMOR with differences noted for those patients whose slope was detected differently, see Appendix C Figure C.2. An overarching trend in fall on the side boundary conditions is the positive % change as opposed to stance position where a negative % change trend was noted. It appears that, when assigning these boundary conditions, a lower resolution is associated with stronger bones rather than weaker.

A consistent outlier in the neck and trochanter posterior regions was noted for patient 2's right femur and is most likely due to the atypical geometry as noted before. This does not justify the large difference seen in patient 2's left femur, for Fall E in the trochanter posterior and anterior, which had typical femoral bone geometry and was reconstructed properly. A large difference in slope was noted, however, in patient 2 which may account for this larger percent change for the left femur as well as emphasizing the % change in the right femur. Patients 10 and 18 had a large percentage change in slope as well, and though this may account for the larger percent change in stains, these large differences were also seen in similar patients such as patient 9 in Fall A trochanter anterior, where patient 9 had a 0% change in slope. Further investigation is warranted in assessing how these slopes impact strains in *Simfini-SENIOR* when specifically looking at short bones.

When comparing *Simfini-TUMOR* and *Simfini-SENIOR* results in stance position one noticed a similar percentage change in strains at the superior neck. Larger changes were seen at the trochanter in *Simfini-SENIOR* analysis in stance position compared to *Simfini-TUMOR*, however these changes were seen for patients where a larger change in slope was also noted, strengthening the conclusion that a better algorithm for slope detected is needed. Patients in *Simfini-TUMOR* that had larger differences in compression strains when comparing CT resolution also had larger differences in *Simfini-SENIOR* in all three applied boundary conditions. We noticed consistent outliers for patient 5 and patient 8, where the difference in slope may explain variations in strain detection for patient 8 in *Simfini-TUMOR* but the same phenomenon was not seen in *Simfini-SENIOR*. The reason for these large variations among these two patients is not clear but may be a result of lytic lesions (softened section of a patient's bone) seen in the cortical bone. Similar to overlooking the cortical shell that impacted bone strength, overlooking lesions that are >1mm longitudinally within the cortical bone may impact interpreted bone strength, although further investigation is warranted.

Bland-Altman plots in Appendix E demonstrate that for all regions within the femur the bias is not proportional to the measurement. The bias itself for the trochanter, proximal shaft, and middle shaft is relatively low ≤6% for stance position and ≤10% for fall on the side with large variations in the upper and lower limit. The bias, similar to the precent change, denotes a consistent deviation between the two paired ST variables that must be taken into account when analyzing the AFE results using lower resolution CT scans.

We conclude that when using stance position loading for CT scans of both 3mm and 1mm ST, the regions of the femur with relatively small changes in the results are the trochanter (-0.1 ± 6.0 %) *, proximal shaft (-3.6 ± 3.7 %) *, and middle shaft (-3.0 ± 2.6 %) *. In these regions an approximate ~ -5% difference can be assumed interpreting a stronger bone compared to the gold standard of 1mm ST/SS. This is especially relevant for longitudinal studies aimed at assessing patient specific bone strength in consecutive CT scans. In such studies any changes above 5% in said regions should be correlated to alterations in bone stiffness. Large variations are noted in the superior neck limiting the ability to note changes in this region below ~10%.

For fall on the side loading for the proximal femurs we note for Fall A the following differences: the superior neck (6.6 ± 12.0%) *, trochanter posterior (3.9 ± 16.4%) *, and lesser trochanter anterior (9.2 ± 16.0 %) *. For Fall E the following are the differences: the superior neck (-0.3 ± 8.4%) *, trochanter posterior (-4.1 ± 11.4%) *, and lesser trochanter anterior (5.5 ± 11.9%) *. For these loading conditions an average difference of below 10% should not be considered as an alteration in bone stiffness.

WBLD CT scans provide adequate insight on femurs' stiffness in the specific regions where a change in bone strains is less than 5% for Stance Position and less than 10% for fall on the side compared with 1mm CT scans. AFEs will be used in a followup longitudinal assessment for SMM patients with WBLD CT scans where biomechanically altered bone would be determined if strains are consistently above the mentioned changed level over a period of time.

Limitations

The number of femurs studied is 24 and a limited statistical analysis of the statistical power of the results has been performed. A larger cohort may provide a better statistical outcome.

* *These averages and STD were calculated based on the outcomes of both the left and right femur.*

Patients' history was not provided, and many of the analyzed femurs had evidence of lytic lesions. The impact of various bone diseases on AFE's outcome is warranted.

Acknowledgments

LE and ZY gratefully acknowledge the many discussions and assistance provided by Mr. Kent Myers of PerSimiO, Beer-Sheva Israel. This research was partially supported by the Medical Research Infrastructure and Health Services Fund of Sourasky MC.

References

1) Yosibash, Z., Plitman Mayo, R., Dahan, G., Trabelsi, N., Amir, G., Milgrom, C., 2014. Predicting the stiffness and strength of human femurs with real metastatic tumors. Bone 69, 180–190. https://doi.org/10.1016/j.bone.2014.09.022
2) Yosibash, Z., Myers, K., Trabelsi, N., Sternheim, A., 2020. Autonomous FEs (AFE) - A stride toward personalized medicine. Computers & Mathematics with Applications, 2019 80, 2417–2432. https://doi.org/10.1016/j.camwa.2020.03.012
3) Sternheim, A., Traub, F., Trabelsi, N., Dadia, S., Gortzak, Y., Snir, N., Gorfine, M., Yosibash, Z., 2020. When and where do patients with bone metastases actually break their femurs? Bone Joint J 102-B, 638–645. https://doi.org/10.1302/0301-620X.102B5.BJJ-2019-1328.R2
4) Prevrhal, S., Fox, J.C., Shepherd, J.A., Genant, H.K., 2003. Accuracy of CT-based thickness measurement of thin structures: modeling of limited spatial resolution in all three dimensions. Med Phys 30, 1–8. https://doi.org/10.1118/1.1521940
5) Applications [WWW Document], n.d. . PerSimiO. URL https://www.persimio.com/new-page-5 (accessed 11.24.20).
6) Ford, J.M., Decker, S.J., 2016. Computed tomography slice thickness and its effects on three-dimensional reconstruction of anatomical structures. Journal of Forensic Radiology and Imaging, Special Issue: Papers from the ISFRI Conference 2015 4, 43–46. https://doi.org/10.1016/j.jofri.2015.10.004
7) Trabelsi, N., Yosibash, Z., Wutte, C., Augat, P., Eberle, S., 2011. Patient-specific finite element analysis of the human femur--a double-blinded biomechanical validation. J Biomech 44, 1666–1672. https://doi.org/10.1016/j.jbiomech.2011.03.024
8) Kivelson, M.G., Russell, C.T., 1995. Introduction to Space Physics [WWW Document]. Higher Education from Cambridge University Press. https://doi.org/10.1017/9781139878296
9) Benca, E., Amini, M., Pahr, D.H., 2020. Effect of CT imaging on the accuracy of the finite element modelling in bone. European Radiology Experimental 4, 51. https://doi.org/10.1186/s41747-020-00180-3
10) Trabelsi, N., & Yosibash, Z. “Patient-specific finite-element analyses of the proximal femur with orthotropic material properties validated by experiments.” J Biomechanical Eng, 133(6) (2011).
11) Treece, G.M., Poole, K.E.S., Gee, A.H., 2012. Imaging the femoral cortex: Thickness, density and mass from clinical CT. Med Image Anal 16, 952–965. https://doi.org/10.1016/j.media.2012.02.008

12) Holzer, G., von Skrbensky, G., Holzer, L.A., Pichl, W., 2009. Hip fractures and the contribution of cortical versus trabecular bone to femoral neck strength. J Bone Miner Res 24, 468–474. https://doi.org/10.1359/jbmr.081108
13) Sternheim, A., Giladi, O., Gortzak, Y., Drexler, M., Salai, M., Trabelsi, N., Milgrom, C., Yosibash, Z., 2018. Pathological fracture risk assessment in patients with femoral metastases using CT-based finite element methods. A retrospective clinical study. Bone 110, 215–220. https://doi.org/10.1016/j.bone.2018.02.011
14) Gholami, M., Karami, V., 2018. Addressing as Low as Reasonably Achievable (ALARA) in Pediatric Computed Tomography (CT) Procedures. Journal of Research in Medical and Dental Science 6, 104–114.
15) Piao, S., Liu, J., 2019. Accuracy Improvement of UNet Based on Dilated Convolution. J. Phys.: Conf. Ser. 1345, 052066. https://doi.org/10.1088/1742-6596/1345/5/052066
16) Rotman, D., Ariel, G., Rojas Lievano, J., Schermann, H., Trabelsi, N., Salai, M., Yosibash, Z., Sternheim, A., 2021. Assessing hip fracture risk in type-2 diabetic patients using CT-based autonomous finite element methods : a feasibility study. Bone Joint J 103-B, 1497–1504. https://doi.org/10.1302/0301-620X.103B9.BJJ-2020-2147.R1
17) Kazley, J.M., Banerjee, S., Abousayed, M.M., Rosenbaum, A.J., 2018. Classifications in Brief: Garden Classification of Femoral Neck Fractures. Clin Orthop Relat Res 476, 441–445. https://doi.org/10.1007/s11999.0000000000000066
18) Keyak, J.H., Skinner, H.B., Fleming, J.A., 2001. Effect of force direction on femoral fracture load for two types of loading conditions. J Orthop Res 19, 539–544. https://doi.org/10.1016/S0736-0266(00)00046-2
19) Romano, A., Cerchione, C., Conticello, C., Martinelli, G., Di Raimondo, F., 2020. How we manage smoldering multiple myeloma. Hematol Rep 12, 8951. https://doi.org/10.4081/hr.2020.8951
20) Rajkumar, S.V., 2020. Multiple myeloma: 2020 update on diagnosis, risk-stratification and management. American Journal of Hematology 95, 548–567. https://doi.org/10.1002/ajh.25791
21) Cohen, Y.C., Avivi, I., Yosibash, Z., Trabelsi, N., Sherman, H., Sternheim, A., 2017. Novel CT-Based Bone Strength Assessment By Finite Element Analysis for Monitoring Bone Involvement in Myeloma: a Proof of Concept Study. Blood 130, 3143. https://doi.org/10.1182/blood.V130.Suppl_1.3143.3143
22) Yekutiel Katz, Nir Trabelsi and Zohar Yosibash, 2022. Automatic femur segmentation from CT scans for autonomous finite element analyses. Submitted for publication.

23) Bolli, N., Sgherza, N., Curci, P., Rizzi, R., Strafella, V., Delia, M., Gagliardi, V.P., Neri, A., Baldini, L., Albano, F., Musto, P., 2021. What Is New in the Treatment of Smoldering Multiple Myeloma? Journal of Clinical Medicine 10, 421. https://doi.org/10.3390/jcm10030421

24) Kristinsson, S.Y., Minter, A.R., Korde, N., Tan, E., Landgren, O., 2011. Bone disease in multiple myeloma and precursor disease: novel diagnostic approaches and implications on clinical management. Expert Rev Mol Diagn 11, 593–603. https://doi.org/10.1586/erm.11.44

25) Hjorth, M., Hellquist, L., Holmberg, E., Magnusson, B., Rödjer, S., Westin, J., 1993. Initial versus deferred melphalan-prednisone therapy for asymptomatic multiple myeloma stage I - A randomized study. Myeloma Group of Western Sweden. Eur J Haematol 50, 95–102. https://doi.org/10.1111/j.1600-0609.1993.tb00148.x

26) Mateos, M.-V., Hernández, M.-T., Giraldo, P., de la Rubia, J., de Arriba, F., Corral, L.L., Rosiñol, L., Paiva, B., Palomera, L., Bargay, J., Oriol, A., Prosper, F., López, J., Olavarría, E., Quintana, N., García, J.-L., Bladé, J., Lahuerta, J.-J., San Miguel, J.-F., 2013. Lenalidomide plus Dexamethasone for High-Risk Smoldering Multiple Myeloma. New England Journal of Medicine 369, 438–447. https://doi.org/10.1056/NEJMoa1300439

27) 27 Mateos, M.-V., Kumar, S., Dimopoulos, M.A., González-Calle, V., Kastritis, E., Hajek, R., De Larrea, C.F., Morgan, G.J., Merlini, G., Goldschmidt, H., Geraldes, C., Gozzetti, A., Kyriakou, C., Garderet, L., Hansson, M., Zamagni, E., Fantl, D., Leleu, X., Kim, B.-S., Esteves, G., Ludwig, H., Usmani, S., Min, C.-K., Qi, M., Ukropec, J., Weiss, B.M., Rajkumar, S.V., Durie, B.G.M., San-Miguel, J., 2020. International Myeloma Working Group risk stratification model for smoldering multiple myeloma (SMM). Blood Cancer J 10, 102. https://doi.org/10.1038/s41408-020-00366-3

28) 28 Merz, M., Hielscher, T., Schult, D., Mai, E.K., Raab, M.S., Hillengass, J., Seckinger, A., Hose, D., Granzow, M., Jauch, A., Goldschmidt, H., 2020. Cytogenetic subclone formation and evolution in progressive smoldering multiple myeloma. Leukemia 34, 1192–1196. https://doi.org/10.1038/s41375-019-0634-2

29) Birnbaum, B.A., Hindman, N., Lee, J., Babb, J.S., 2007. Multi-detector row CT attenuation measurements: assessment of intra- and interscanner variability with an anthropomorphic body CT phantom. Radiology 242, 109–119. https://doi.org/10.1148/radiol.2421052066

30) Eggermont, F., Verdonschot, N., Linden, Y. van der, Tanck, E., 2019. Calibration with or without phantom for fracture risk prediction in cancer patients with femoral bone metastases using CT-based finite element models. PLOS ONE 14, e0220564. https://doi.org/10.1371/journal.pone.0220564

31) Ataei, A., Eikhout, J., van Leeuwen, R.G.H., Tanck, E., Eggermont, F., 2022. The effect of variations in CT scan protocol on femoral finite element failure load assessment using phantomless calibration. PLoS One 17, e0265524. https://doi.org/10.1371/journal.pone.0265524
32) Katz Y., Dahan G., Sosna J., Shelef I., Cherniavsky E. and Yosibash Z., 2019, Scanner influence on the mechanical response of QCT-based finite element analysis of long bones, J Biomech, 86, 149–159, (2019)

Appendix A

Figure A.1 provides the % change for total head displacement and bone stiffness. In these graphs patients 2 and 8 stand out have a larger % change in displacement at the head center and bone stiffness. The distance from the head center to the intercondylar notch was calculated by (9) and plotted in appendix A Figure A.2. This distance affects the loading vector. A greater deviation in distance is noted in patient 10, however this appeared negligent in effecting stains. Thus, anatomical loading conditions don't appear largely impacted due to lower resolution. Larger variations are similarly noted in tension and compression. Figure A.3 presents the compression strains of the inferior neck/subcapital (IN/S), trochanter (T), proximal shaft (PS), middle shaft (MS), and distal shaft (DS) were computed from 3mm to 1mm by (7), E3 denotes the minimal principal strain (compression) at every given region *i*= IN/S, T, PS, MS, DS. The total head displacement (U_{TotHd}) and bone stiffness (BS) were compared from 3mm to 1mm by A(1) and A(2) respectively. These results, in terms of the difference between 3mm and 1mm scans, are similar to those of tension as expected.

$$(17)\ Diff_{TotHd} = \left(\left(\frac{U_{TotHd}|_{3mm} - U_{TotHd}|_{1mm}}{U_{TotHd}|_{1mm}}\right)\right) \times 100$$

$$(18)\ Diff_{BS} = \left(\left(\frac{K_{BS}|_{3mm} - K_{BS}|_{1mm}}{K_{BS}|_{1mm}}\right)\right) \times 100$$

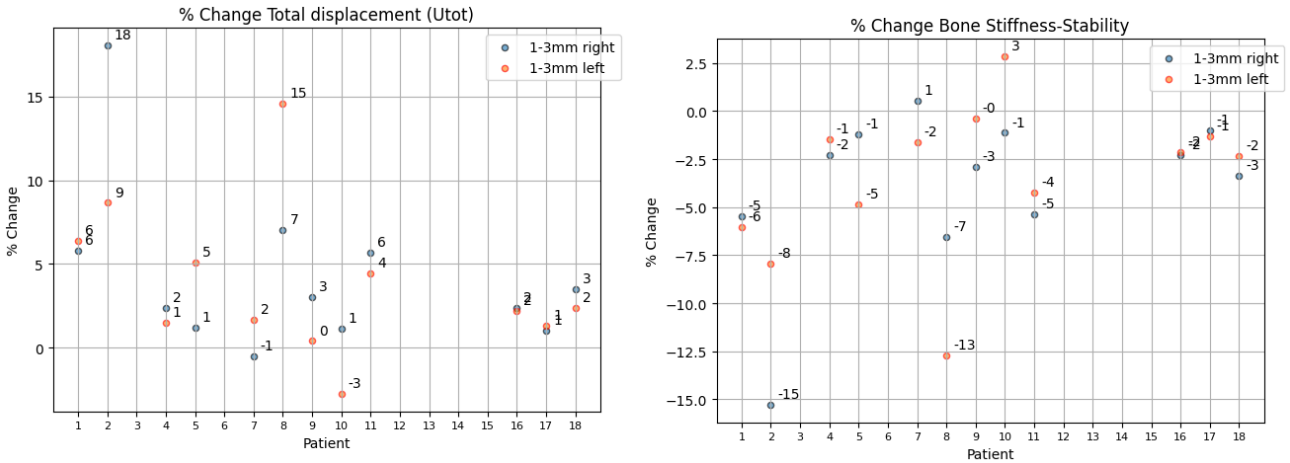

Figure A.1 Total displacement of the head center and bone stiffness.

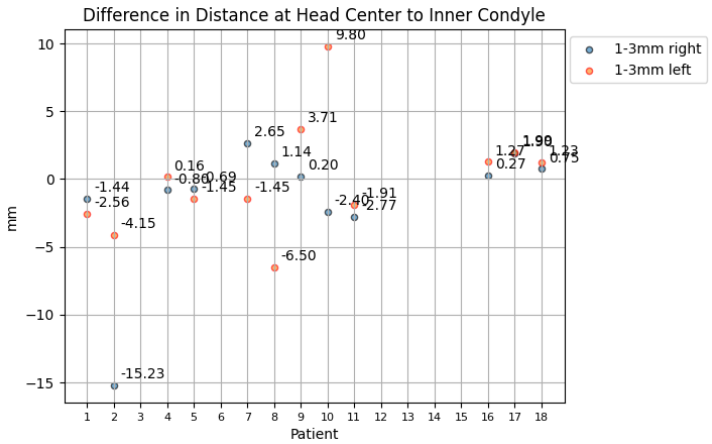

Figure A.2. The change in distance (in millimeters) from the head center to the intercondylar notch.

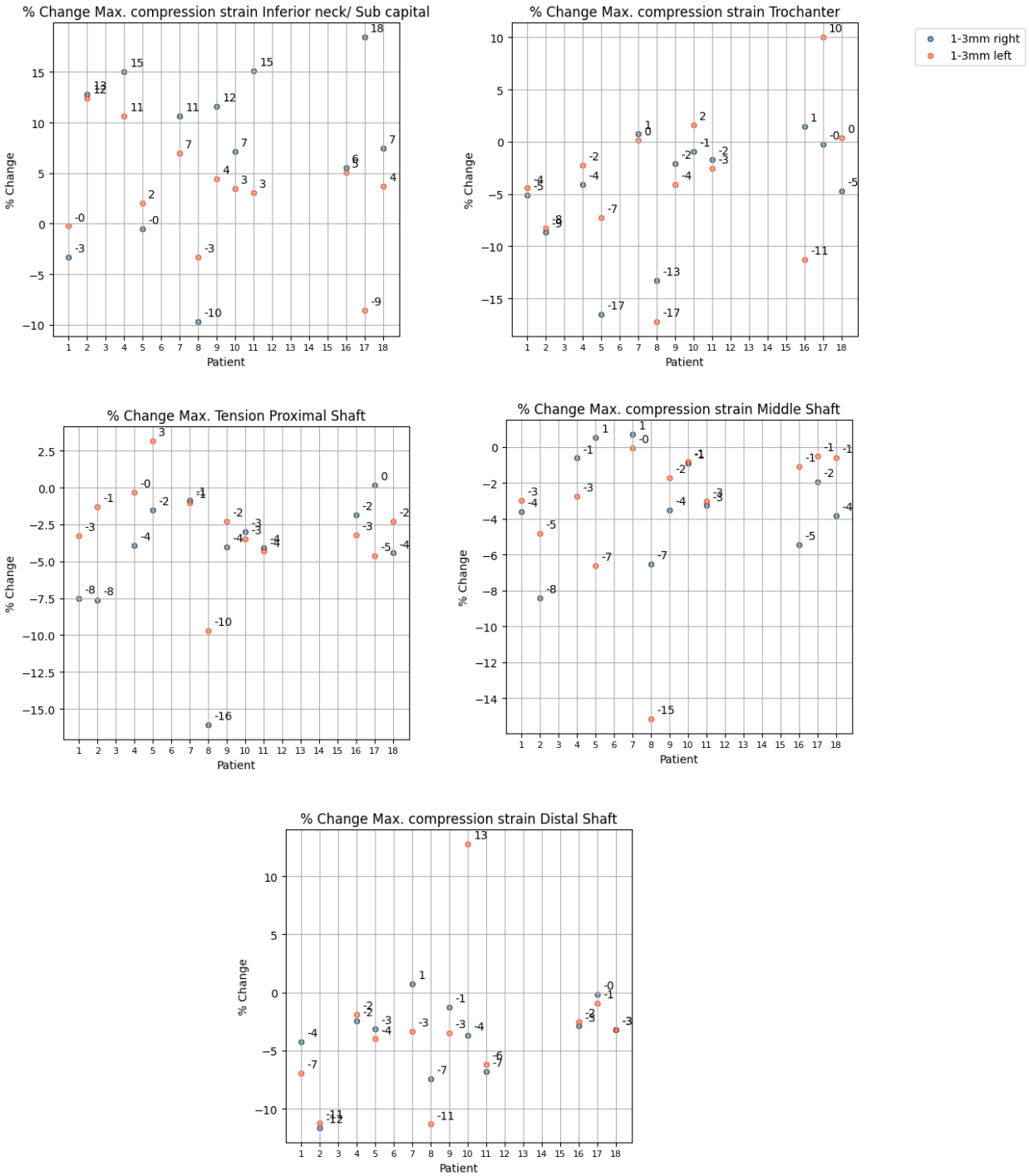

Figure A.3 Percent change of E3 (compression) of the superior neck, trochanter, proximal shaft, middle shaft, and distal shaft for each segmented femur.

Appendix B

As Simfini is an automated system, an algorithm is in place to automatically assess CT scan pixels with the highest HU values to calculate a slope in phantomless CT scans. This slope allows for a correlation between HU and longitudinal Young's modulus which then assigns inhomogeneous isotropic material properties at each voxel along the femur. Patient 8 FEA analysis resulted in a 5% change in slope calculation when comparing CT scans of 1 and 3mm ST. We wanted to assess the impact of the automatic calculation of slope on the resulting strains to generate an understanding on how greatly this 5% difference impacts our results. The analysis was rerun for patient 8 where the slope calculated during the 1mm analysis, of 0.7179, was manually changed whilst running the 3mm analysis (overriding the automated calculation A comparison of % change in strains for patient 8 before and after augmentation of the slope is provided, see Figure B.1(left) for tension and Figure B.1(right) for compression, difference at head center, and bone stiffness. In almost all regions a better correlation between the different CT scan resolution is noted. In the left trochanter rather than a -3% difference a 5% difference is noted, signifying that a slightly weaker bone is estimated in this reason rather than a slightly stronger. This difference is negligent as it is in the bounds of results interpreted for previous patients. The results noted here demonstrate the impact of (an even slightly) altered slope. This warrants an update to the algorithm assessing slope, especially for fall on the side boundary conditions where short bones are used. Currently *Simfini's* algorithm assesses the largest HU of the left femur to determine the slope used for both left and right bone, in some cases different slopes were calculated for the right bone which is overridden for the slope used for the left bone. Possibly interpreting the pixels with largest HU in both bones and then determining the slope to be used for both bones could provide more consistency.

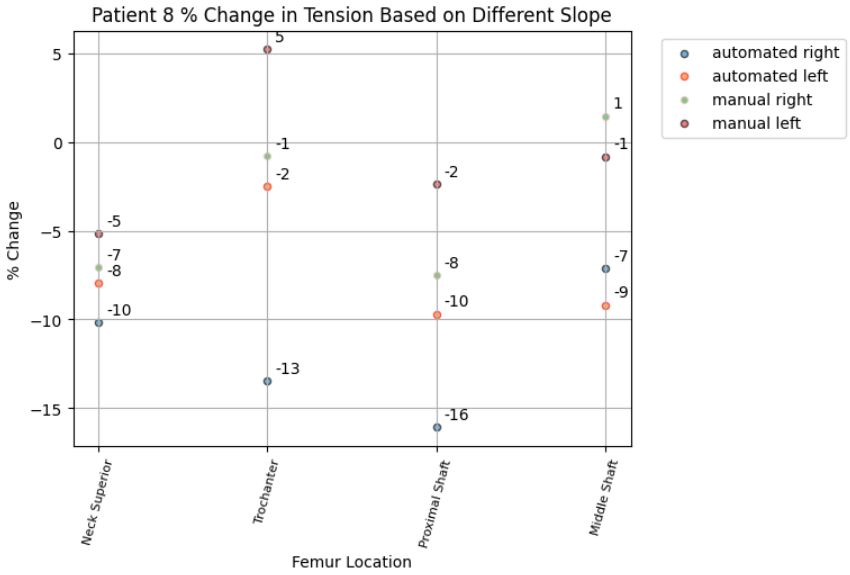

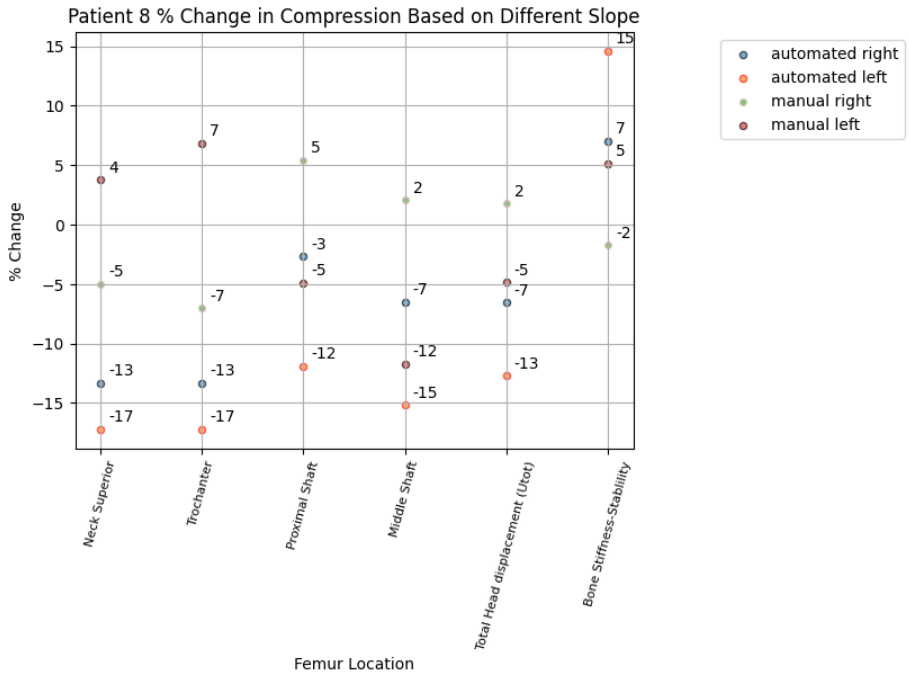

Figure B.1 Tension, compression, total displacement at the head center, and bone stiffness/stability graphs for patient 8 with autonomously calculated slope for both 1 & 3mm analysis compared with manually inputted slope of 0.71789917 calculated based on the 1mm CTFEA. Results for patient 8 are reported based on manually inserted slope so that the FEA 3mm ST analysis will be assessed with the same slope used for the FEA 1mm ST analysis.

Appendix C

Here results for *Simfini*-SENIOR in stance position are provided. Figure C.1 provides the % change for The total head displacement (U_{TotHd}) and bone stiffness (BS) compared from 3mm by Appendix A equation A(1) & A(2) respectively. In these graphs patient 2 and 8 standout have larger % change in displacement at the head center (left) and bone stiffness (right). Here larger variations are noted for displacement at the head center for patients 2, 10 & 18 all of which had a larger % difference in slope between 1 and 3mm ST. Figure C.2 present the tension and compression strains of the superior neck (SN), inferior neck/subcapital (IN/S), trochanter (T), proximal shaft (PS), middle shaft (MS), and distal shaft (DS) were computed from 3mm to 1mm by (6) & (7) respectively. E1 represents the average maximum principal strain (tension) at every given region *i*= SN, T, PS, MS, DS. E3 denotes the minimal principal strain (compression) at every given region *i*= IN/S, T, PS, MS, DS. These results, in terms of difference between 3mm and 1mm scans, are somewhat similar to those of tension as expected. Patient 5 and 8 results in larger varying compression strains compared to tension, both patients were noted to show larger differences in stains along all boundary conditions in *Simfini*-SENIOR.

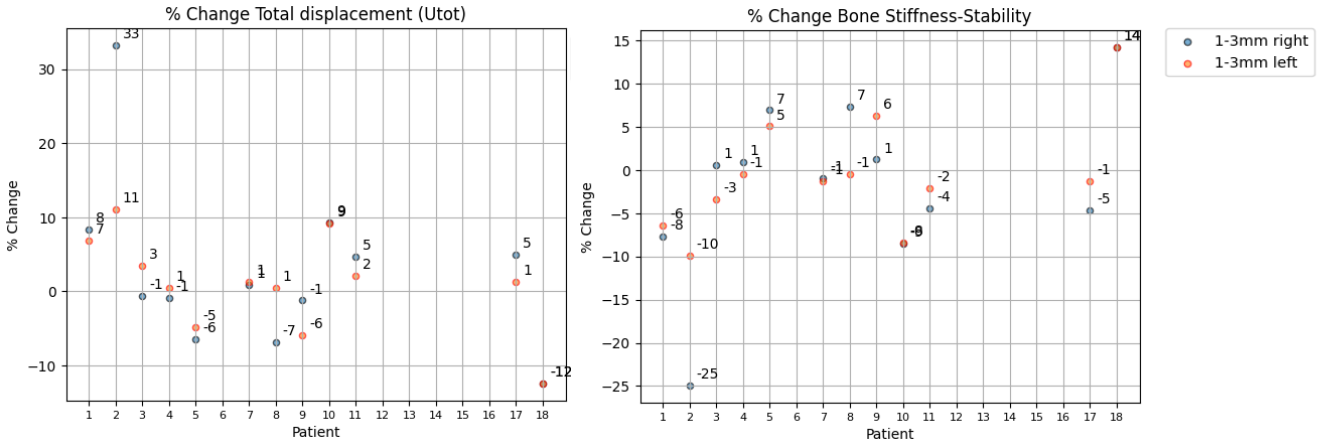

Figure C.1 Total displacement of the head center and bone stiffness.

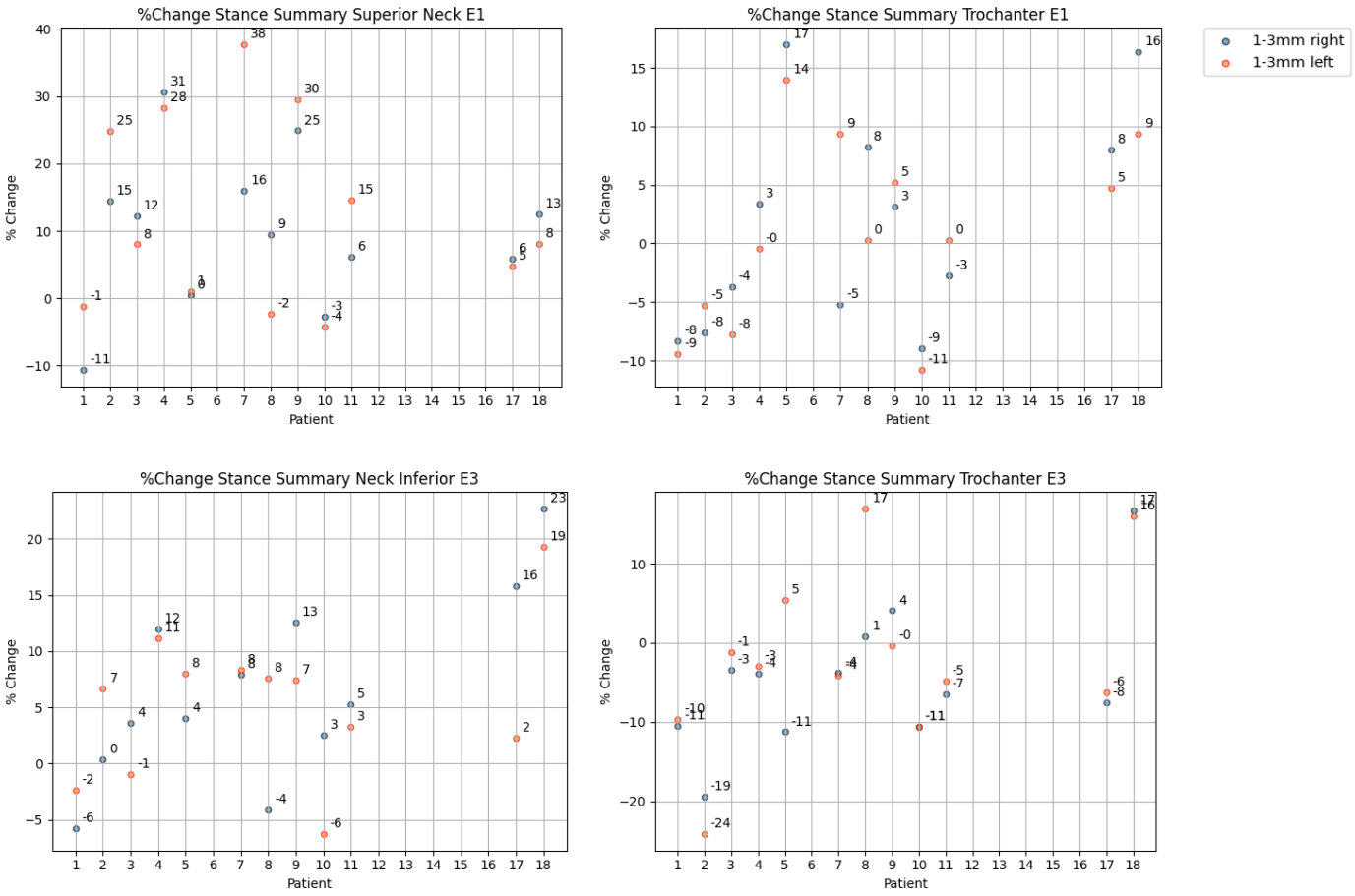

Figure C.2. Percent change of E1 (tension) & E3 (compression) of the superior neck and trochanter of short bones for each segmented femur with fall on the side loading.

Appendix D

U-Net algorithm for the segmentation of a femur in the CT-scan are presented in this Appendix. U-Net detects the slice that represents the end of the femur, as seen in Figure D.1d for stance position, the slice that represents the end of the femoral head, Figure D.1c and thereafter the femurs are segmented, see Figure D.1b. Figure D.2 shows the difference in the segmented femur's-length if 1mm and 3mm scans are used. Figure D.3 shows the tumors in femur's head for both 1mm and 3mm ST CT scans so the automatic segmentation could not detect the beginning of femoral head properly - see Figure D.2.

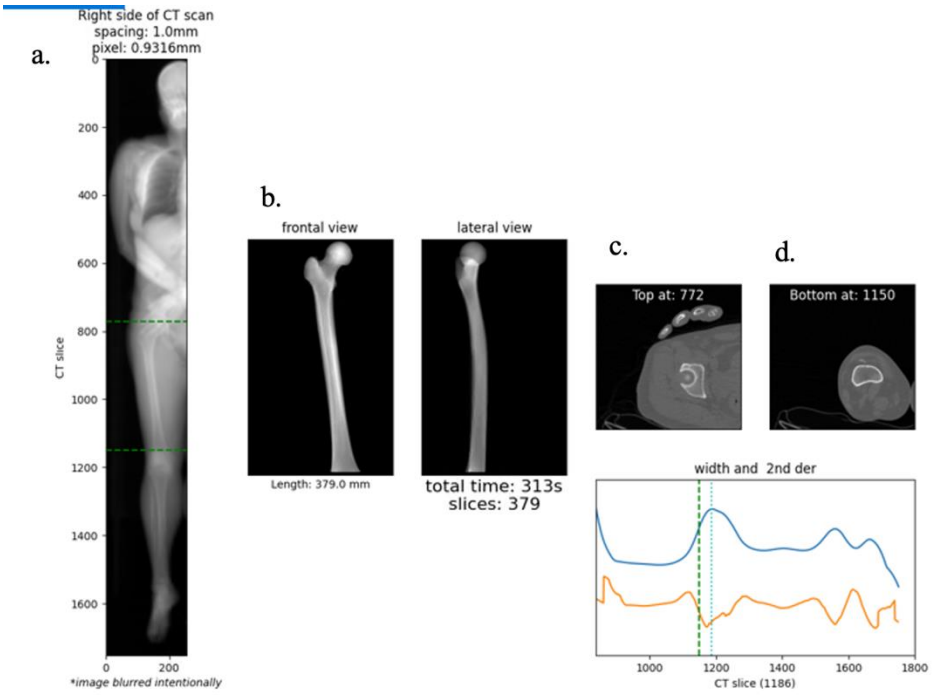

Figure D.1. The output file after femur segmentation of the right femoral bone denotes the slice range of the femur. A) Right half of a CT scan and the detection of the femur in the WBCT, b) Segmented femur frontal and lateral view, providing the length of the bone, slices range, and total time to segment, c) 2D slice of the femoral head before reaching the pelvis, detected after being fed into the U-net system, d) 2D slice detected right above the patella being the last slice of the femur during segmentation, a boundary condition was applied as though the femur was clamped at the bottom of the distal shaft. E) the graph shows two curves that represent the width of the femoral bone from the pelvis to the end of the WBLD CT scan and the second derivative of the width. The large convex curve seen in the graph around slice 1200 signifies the knee bone. This was how the U-net detected the knee and "knew" how to detect the last slice before the patella, which is noted as the dashed green line on the graph and the CT slice used denoting the last slice is written under the graph "CT slice (1186)".

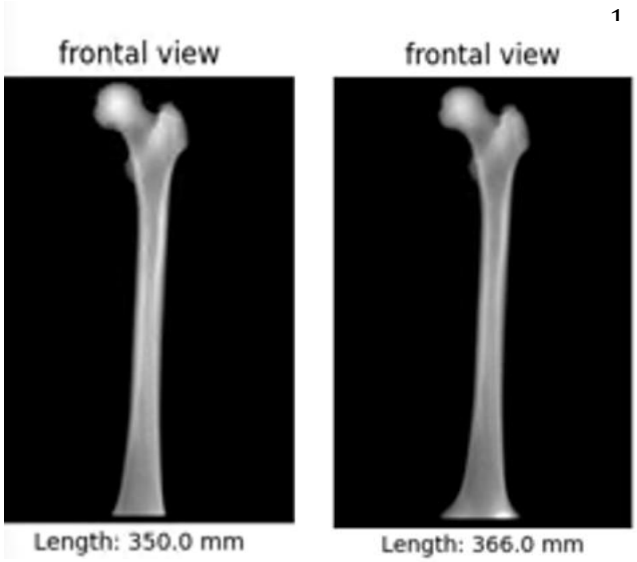

Figure D.2. A frontal view of both segmented left femurs of patient 10, Left) 1mm Right) 3mm. Femoral bone in 3mm scan is segmented with a part of the knee.

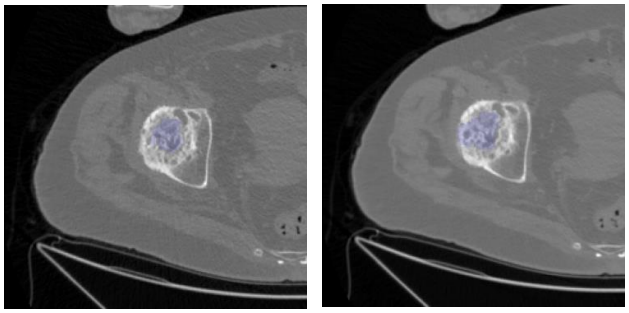

Figure D.3. The first slice detecting the start of the femoral head for patient 2 Left) 1mm Right) 3mm. The purple region denotes the area that *Simini* automatically selected as femoral bone. Both instances fail to properly extract femoral bone due to the many tumors. A slightly larger region is extracted in the 3mm ST CT scan compared to the 1mm.

Appendix E

Bland Altman plots are presented for the visualization of a bias and if the bias is proportional to the measurement. It is difficult to decern if the outliers, causing the large deviations, detected along various regions are consistent with one patient.

A constant bias is noted for all regions for stance position and fall on the side. The bias, lower and upper limits as a percent deviation based on the difference of means are noted in Table E.1. For stance position a constant bias of ≤6% is noted for the trochanter, proximal shaft, and middle shaft in tension and compression with larger stand deviations, whereas the superior neck and distal shaft result in larger biases with a larger standard deviation, as seen in the previous measurements. Whereas a constant bias of ≤10% for fall on the side is noted. These results indicate that a bias should be considered when using lower resolution CT scans, but as the bias can be quantified, such scans can be used for CTFEA to predict patient bone's strength.

$$(19)\ Bias_i = \frac{1}{n}\sum_{j=1}^{n}(Diff_i)_j$$

$$(20)\ Limits\ of\ agreement_i = (Bias_{i\pm}\ 1.96\ \ Standard\ \text{Deviation}_i)_j$$

$Standard\ \text{Deviation}_i$ was calculated by equation (16).

Where i=location, $Diff_i$= the difference in strain value from 1mm to 3mm of the patient, (j) at each location (i), $\bar{x}$= the mean of $Diff_i$, and n= total number of femurs.

23

Table F.1 Bland Altman plot depicting mean difference at each location for 1mm and 3mm ST in *Simfini-TUMOR and Simfini-SENIOR*. Calculations by (19) & (20).

		Femurs	n = 24			
		Femur Loction	% Bias	% SD upper	% SD lower	Diversely Proportional to Measurement
Stance Position	E1	Superior Neck	-8.9	13.2	-31.2	x
	E1	Trochanter	-0.08	18.8	-18.8	x
	E1	Proximal Shaft	4	11.7	-3.9	x
	E1	Middle Shaft	3.1	7.7	-1.5	x
	E1	Distal Shaft	-2.5	60	-64	x
	E3	Superior Neck	-6.6	-25.5	12.5	x
	E3	Trochanter	6.1	-12.5	24.4	x
	E3	Proximal Shaft	4.1	-8.6	16.6	x
	E3	Middle Shaft	5.9	-7	18.8	x
	E3	Distal Shaft	-7.3	-13.6	28	x
Fall A	E3	Neck Superior	-3.3	-15.8	9.2	x
	E3	Trochanter Poste	-2.8	-30	23.3	x
	E3	Trochanter Anter	-10	-43	23	x
Fall E	E3	Neck Superior	0.09	-10.7	10.7	x
	E3	Trochanter Poste	5.8	-21.4	32.9	x
	E3	Trochanter Anter	-6.6	-37.1	23.1	x

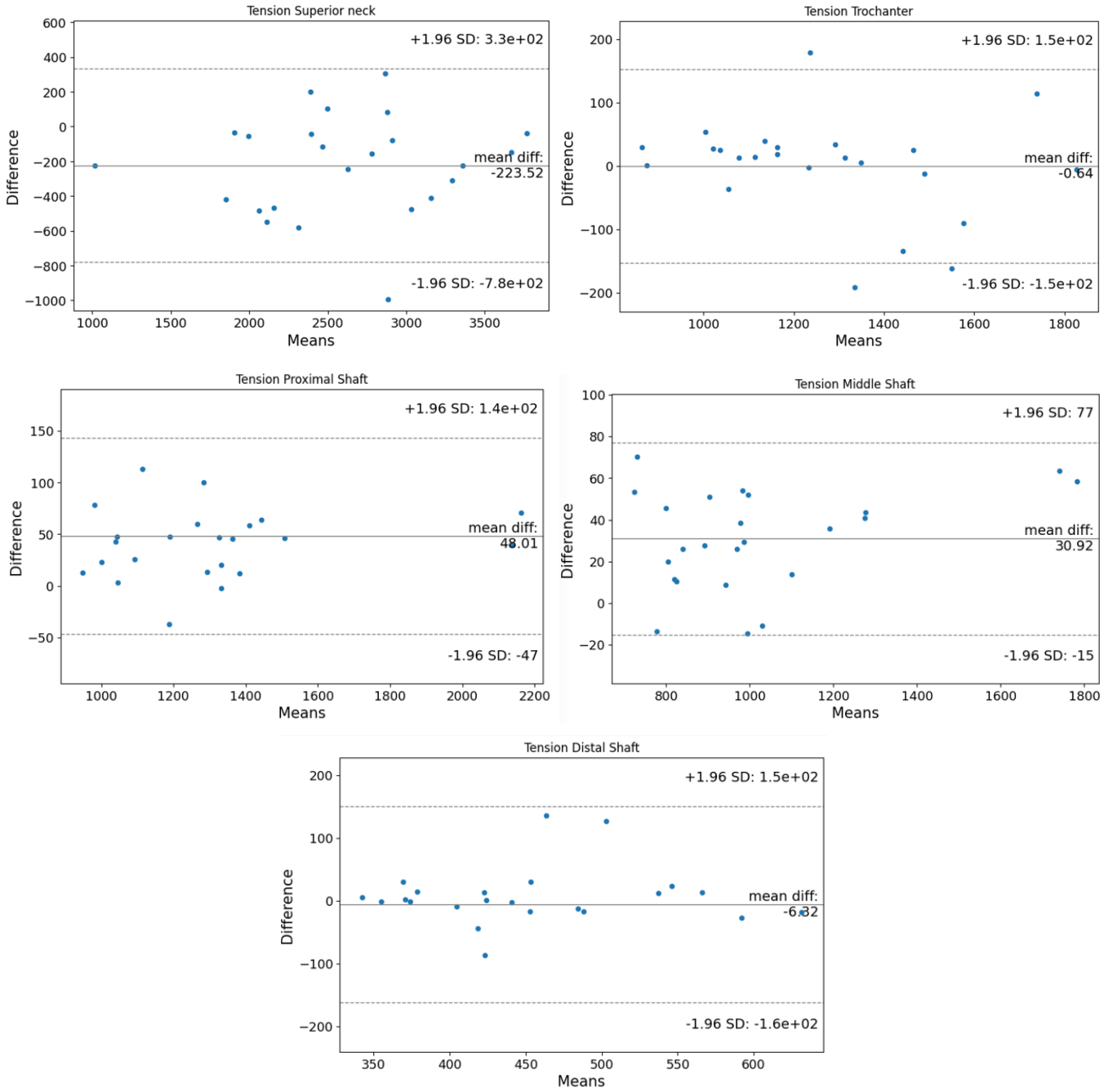

Figure E.1. Bland Altman plots E1 (tension) of the superior neck, trochanter, proximal shaft, middle shaft, and distal shaft for each segmented femur.

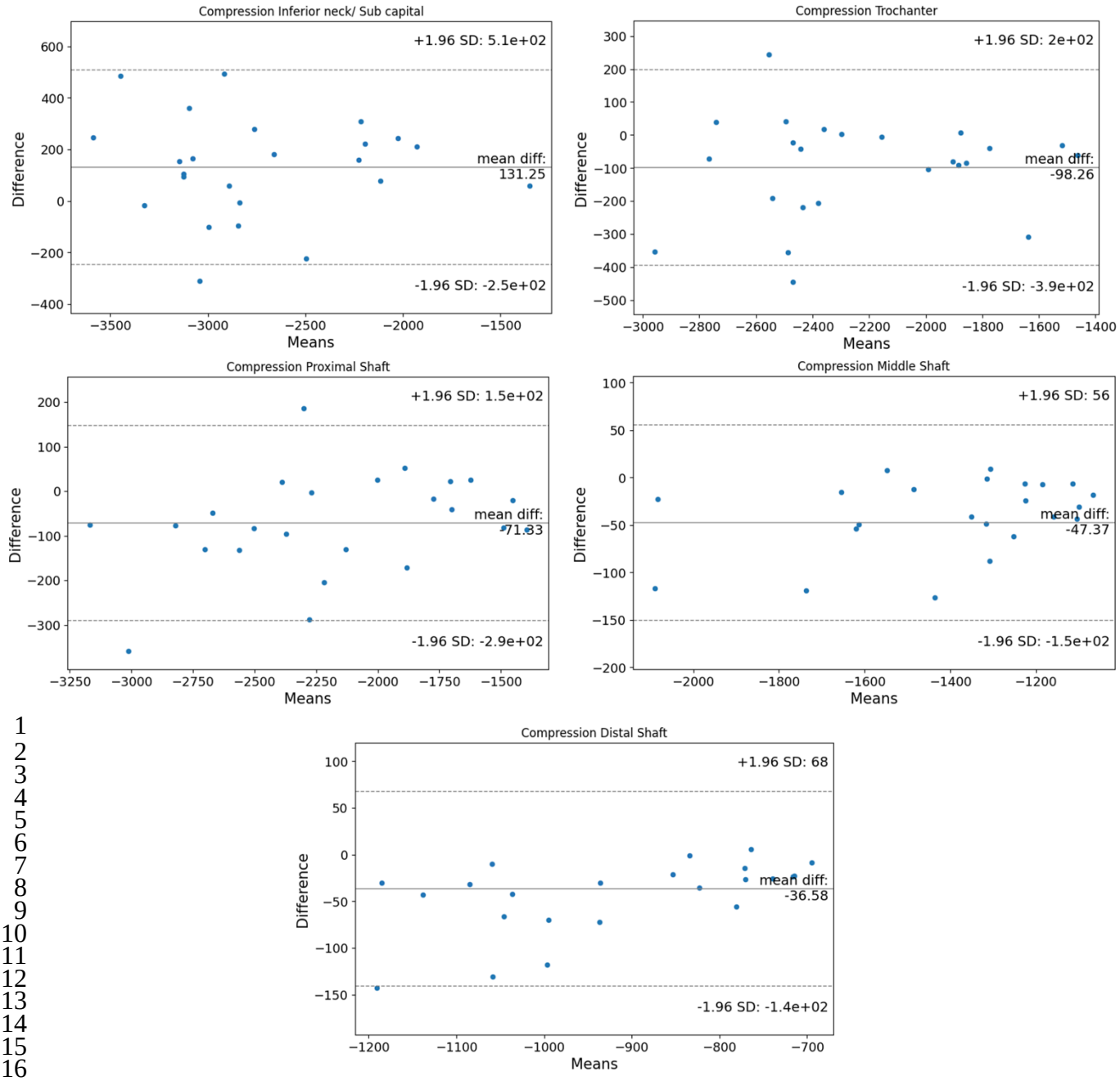

Figure E.2. Bland Altman plots E3 (compression) of the superior neck, trochanter, proximal shaft, middle shaft, and distal shaft for each segmented femur.

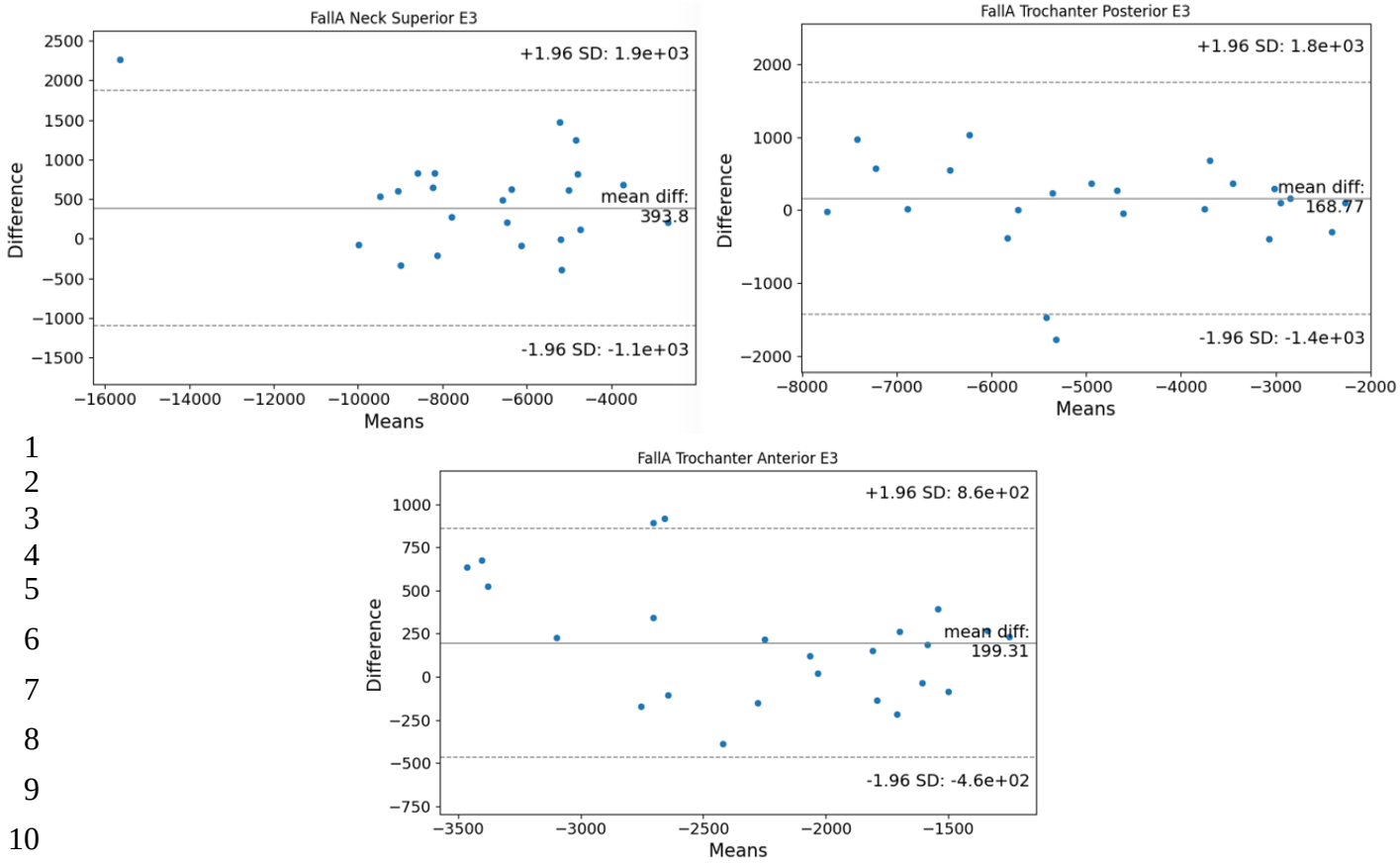

Figure E.3. Bland Altman plots E3 (compression) at Fall A loading conditions at the superior neck, trochanter posterior, and trochanter anterior for each segmented femur.

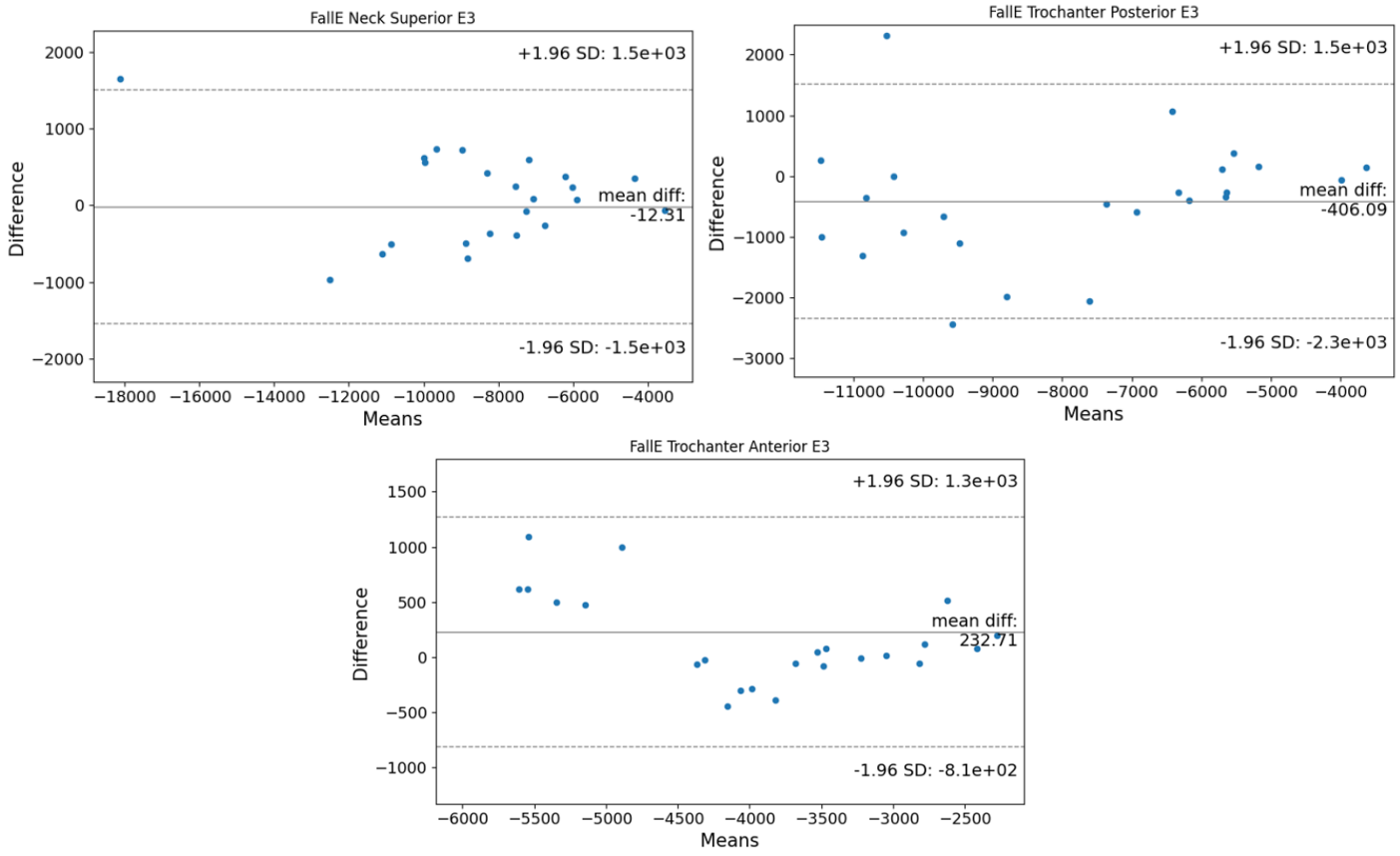

Figure E.4. Bland Altman plots E3 (compression) at Fall E loading conditions at the superior neck, trochanter posterior, and trochanter anterior for each segmented femur.